Silicon Nanostructure Photovoltaics

Thesis by

Douglas Weng Wah Tham

In Partial Fulfillment of the Requirements

for the Degree of Doctor of Philosophy

California Institute of Technology

Pasadena, California

2012

(Defended October 31, 2011)

To my wife and family

Acknowledgements

First of all, I would like to thank my advisor, Professor James Heath, for all the guidance and support he has provided to me. He took me into the group very quickly after I arrived at Caltech and assisted tremendously in my application for the KAUST Scholarship. Jim has been very patient through troubled periods when seemingly nothing would work, while making just the kinds of suggestions that helped to focus my work. Without Jim's help, this work would certainly not have been possible. I would be remiss to not also thank the rest of my committee for giving me a really tough time during my candidacy, and for their great questions during my prop exams. Thank you, Professors Sossina Haile, Nathan Lewis, and Harry Atwater. Not to forget, thank you to my funding agency KAUST and their fine folks who have been taking care of all the little details so that I may be able to concentrate on my work.

At the same time, I would like to express my heartfelt appreciation to all Heath group members, past and present, whom I have had the honor and privilege to cross paths with. There is so much to be thankful for: I have had the opportunity to be immersed in an environment where open critical thought is readily accepted, and where ideas are freely shared without restraint. I am grateful to all of you for contributing to that environment. Thank you especially to my colleagues Akram Boukai (who was somewhat of an instigator of this entire work); Jen-Kan Yu and Slobodan Mitrovic (whom I worked with on silicon thermoelectrics); Ruo-Gu Huang (silicon nanowire transistors); Peigen Cao and Joey Varghese (graphene-templated imaging). I would also like to mention Diane Robinson, for always being able to take time off to talk; Kevin Kan, for his tireless

efforts in maintaining the laboratories; Habib Ahmad, Ke Xu, Dunwei Wang, Jonathan Green, and Bonnie Sheriff, for all their assistance on device processing. Over at the department machine shop, Mike Roy and Steve Olson have always impressed me with great careful and conscientious work, without which my entire measurement platform would not have been possible.

In the broader Caltech community, I would like to thank my good friends for their assistance, critique, know-how and their general awesomeness: Gregory Kimball, Pia Ghosh, Jingqing Huang, Jeff LeHew, Toni Lee, Soyoung Park, Andrej Svorencik, and Marjan Praljak. Never have I met such a diverse set of people with whom I have been able to talk science one second and nonsense in the next. I have had so much fun and memorable moments with this bunch over the past few years.

Last but not least, I would like to thank my family for their love and support over the course of my graduate career. They are the true heroes behind it all who have been always quietly supportive of the work I do, even when I neglect to call for months at a time. To my other family, thank you for opening your hearts to me, and for giving your son-in-law your utmost care and concern without reservation. Above all, to the woman who is my wife, thank you. Without you, none of this would mean anything.

Abstract

Photovoltaic devices consisting of highly periodic, ultradense, silicon nanowire arrays and nanohole arrays have been fabricated with nominal nanowire widths of 20 nm, nanohole sizes of 12 nm, and lattice pitches of 32 nm, deep in the subwavelength regime for visible light. We have developed a set of surface passivation protocols that provide the extremely low surface recombination velocities typical of thick, high-quality, furnace-grown thermal silicon dioxide, but within an ultrathin layer on the order of 5 – 10 nm thick. With this high quality oxide passivation, these devices exhibit good photovoltaic performance that rivals or exceeds all comparable devices reported in the literature. Using a collection of characterization techniques, including optical microscopy, scanning electron microscopy, cross-sectional transmission electron microscopy, and spectroscopic ellipsometry, we characterize the structure and morphology of these nanostructure arrays. The high perfection of the arrays enables absorptance calculations to be performed using rigorous coupled-wave analysis, which solves Maxwell's equations for periodic structures. The calculations show that these deep subwavelength nanostructures behave as homogeneous optical materials with effective refractive indices determined by the structural parameters. We solve approximate models to estimate their refractive indices. When the spectral responses of these devices were measured, their external quantum efficiencies track the calculated absorptances, except for a small multiplicative offset at shorter wavelengths due to a greater than unity internal quantum efficiency, which we estimate by dividing the absorptance into the external quantum efficiency.

Table of Contents

List of Figures

List of Tables

Chapter 1: Introduction

1.1 Limiting Efficiency of Solar Cells

Our Sun is a clean, almost unlimited source of energy that can provide entirely for the energy requirements of the entire planet, if only solar power can be made competitive with competing energy sources. The first-generation crystalline silicon photovoltaic (*c*-Si PV) cell is the predominant technology in the solar cell market; for this type of cell, material costs comprise the bulk of the price per kilowatt-hour generated. Therefore, research in solar power has traditionally focused on reducing the cost of power generation by maximizing the solar conversion efficiency in *c*-Si PV cells. While decades of optimization have produced cells with demonstrated efficiencies of ~24%,[1, 2] conventional approaches to improve c-Si PV cells will not produce performance beyond the limiting efficiency of silicon (~30% under unconcentrated sunlight).

There are two main reasons for the low limiting efficiency of *c*-Si PV cells. First, silicon can only absorb solar photons with energies exceeding the band gap energy of 1.12 eV, corresponding to approximately half of the Sun's total energy output over all photon energies. Second, of the photons that are absorbed, any excess photon energy above the band gap energy is wasted as heat when photoexcited carriers collide with the crystal lattice in carrier-phonon scattering events. The latter "thermalization loss" alone limits the efficiency of the optimum band gap solar cell to 44%.[3]

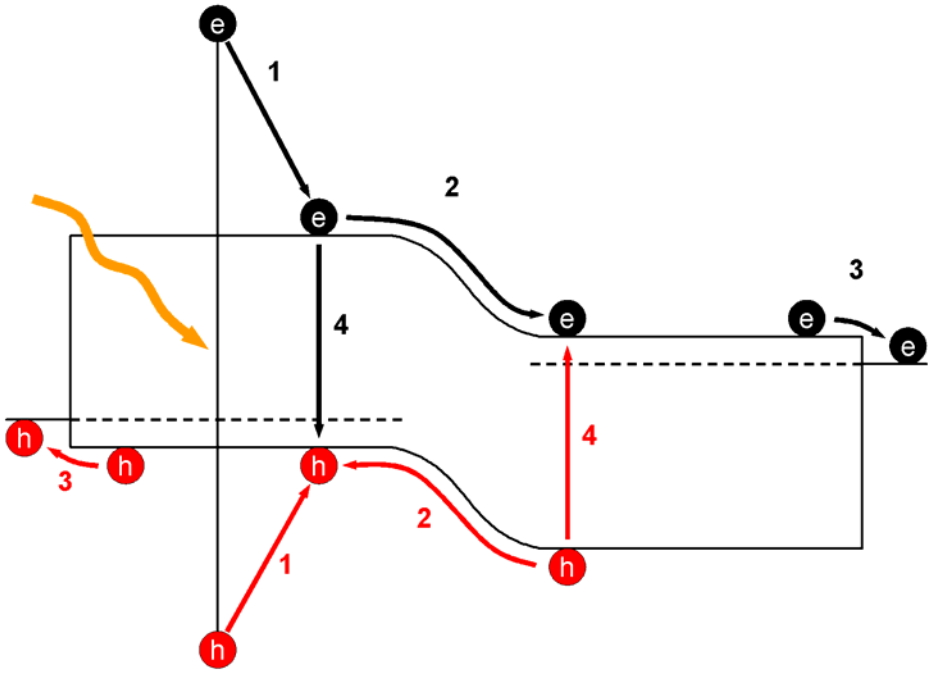

Figure 1-1. Loss mechanisms in a p-n junction solar cell showing energy losses due to (1) carrier thermalization, (2) junction, (3) contacts, and (4) recombination.

Thermalization occurs as follows. When a photon with energy greater than the band gap is absorbed, an energetic ("hot") electron-hole pair is created. The hot carriers possess excess kinetic energy that is readily dissipated into the lattice (figure 1-1, pathway 1). Once the excess kinetic energy is dissipated, the carrier population is said to be "thermalized" and is well represented by two quasi-Fermi distributions for each of the electron and hole populations, with characteristic carrier temperatures determined by the kinetic balance of generation and recombination. If thermalization losses can be reduced, the Shockley-Queisser detailed balance limiting efficiency[4] can be exceeded.

1.2 Tandem Cells to Reduce Thermalization Loss

Smaller band gap materials can be used in a single junction cell to absorb the longer wavelength components of solar radiation, but as the band gap energy moves away from the optimal ~1.3 eV for the standard solar spectrum,[4] the limiting efficiency drops rapidly due to spectral mismatch as well as increased thermalization losses. By extension, one can stack several solar cells with different band gaps in multijunction tandem solar cells, so that the top layer has the largest band gap optimized for the highest energy photons but is transparent to lower energy light. Lower energy photons are transmitted to and absorbed in lower layers that have smaller band gap energies. In this way, one can optimize each cell for a specific part of the solar spectrum so that thermalization losses are reduced in aggregate compared to the single junction solar cell. For a multijunction tandem solar cell with an infinite number of layers, the conversion efficiency approaches ~68% for unconcentrated solar irradiation and ~86% at maximum solar concentration.[5] In practice, cost and material restrictions prevent the fabrication of tandem cells with more than two or three junctions, but this is not problematic as just two or three layers already realize most of the performance gain of the infinite layer stack. Tandem cells with conversion efficiencies above 30% in unconcentrated sunlight are widely available.

An alternative approach is to identify photovoltaic materials for which the thermalization process is sufficiently slow, so that the carriers retain their kinetic energy on a timescale comparable to or longer than the carrier collection time. The additional carrier energy may be utilized in hot carrier solar cells,[6-8] which use energy selective contacts[9, 10] to collect only the higher-energy carriers and produce a higher terminal voltage. Alternatively, these hot carriers may impact ionize[11] and create additional

carriers to produce more current. Indeed, quantum efficiencies above unity have been been observed in bulk Si and Si_x-Ge_{1-x} photovoltaics and attributed to carrier multiplication from impact ionization.[12, 13] Here, we shall limit the following discussion to solar cells of the latter type.

1.3 Nanostructures to Reduce Thermalization Loss

Green has examined potential low-dimensional systems to circumvent thermalization losses in photovoltaics.[3] Nanostructured, low-dimensional photovoltaic materials have been proposed to increase the thermalization time beyond the range of a few picoseconds that is typical for bulk materials. In bulk materials illuminated at high intensities, thermalization times increase because the initial high-energy (optical) phonons carrying the excess carrier energy cannot decay quickly enough into lower-energy (acoustic) phonons that can be readily propagated away. The so-called phonon bottleneck effect is believed to occur more readily in low-dimensional structures because of the restricted density of states that high-energy phonons can decay into. This has motivated explorative studies on various quantum well and quantum dot nanostructures as candidate low thermalization photovoltaic materials. Alternatively, with phononic band gap engineered materials, Brillouin zone folding of the band structure results in a phonon dispersion that exhibits small gaps and a slower speed of sound. Either of these effects can result in enhanced thermalization times: the first restricts the final states that the initial optical phonons can decay into, while the latter slows the propagation of the resulting acoustic phonons away from the local region.[14]

In studies of silicon nanowire[15] and nanohole arrays,[16] we found that these materials exhibited extremely low thermal conductivities, about 2 orders of magnitude lower than the bulk. These results indicate that phonon propagation is significantly slowed in these materials, suggesting the possibility of decreased thermalization losses for photovoltaic devices incorporating silicon nanowire or nanohole arrays. The question is whether nanostructural modifications to silicon reduce the thermalization loss sufficiently that noticeable improvements in carrier multiplication can be observed compared to the unstructured material.

1.4 Summary

In the following chapters we will describe the experimental protocols we used to fabricate our devices (chapter 2), the characterization techniques that were employed (chapter 3), and the modeling that was performed to understand their optical absorption (chapter 4). We move to actual photovoltaic measurements (chapter 5) and show that our devices perform comparably or better than similar devices reported in the literature. Finally, we attempt to answer whether quantum yields can be improved by nanostructuring.

1.5 References

1. Green, M. A.; Zhao, J.; Wang, A.; Wenham, S. R., Very high efficiency silicon solar cells — science and technology. *IEEE Transactions on Electron Devices* **1999,** 46, 1940.

2. Zhao, J.; Wang, A.; Altermatt, P. P.; Wenham, S. R.; Green, M. A., 24% efficient perl silicon solar cell: Recent improvements in high efficiency silicon cell research. *Solar Energy Materials and Solar Cells* **1996,** 41, 87.

3. Green, M. A., Prospects for photovoltaic efficiency enhancement using low-dimensional structures. *Nanotechnology* **2000,** 11, 401.

4. Shockley, W.; Queisser, H. J., Detailed balance limit of efficiency of *p-n* junction solar cells. *Journal of Applied Physics* **1961,** 32, 510.

5. Würfel, P., *Physics of Solar Cells*. Wiley-VCH: Weinheim, 2005.

6. Ross, R. T.; Nozik, A. J., Efficiency of hot-carrier solar energy converters. *Journal of Applied Physics* **1982,** 53, 3813.

7. Würfel, P., Solar energy conversion with hot electrons from impact ionisation. *Solar Energy Materials and Solar Cells* **1997,** 46, 43.

8. Würfel, P.; Brown, A. S.; Humphrey, T. E.; Green, M. A., Particle conservation in the hot-carrier solar cell. *Progress in Photovoltaics* **2005,** 13, 277.

9. Conibeer, G.; Jiang, C.-W.; Green, M.; Harder, N.; Straub, A., Selective energy contacts for potential application to hot carrier PV cells. In *3rd World Conference on Photovoltaic Energy Conversion*, Osaka, Japan, 2003; p 2730.

10. Conibeer, G. J.; Jiang, C.-W.; König, D.; Shrestha, S.; Walsh, T.; Green, M. A., Selective energy contacts for hot carrier solar cells *Thin Solid Films* **2008,** 516, 6968.

11. Landsberg, P. T.; Nussbaumer, H.; Willeke, G., Band-band impact ionization and solar cell efficiency. *Journal of Applied Physics* **1993,** 74, 1451.

12. Kolodinski, S.; Werner, J. H.; Wittchen, T.; Queisser, H. J., Quantum efficiencies exceeding unity due to impact ionization in solar cells. *Applied Physics Letters* **1993,** 63, 2405.

13. Wolf, M.; Brendel, R.; Werner, J. H.; Queisser, H. J., Solar cell efficiency and carrier multiplication in $Si_{1-x}Ge_x$ alloys. *Journal of Applied Physics* **1998,** 83, 4213.

14. Conibeer, G. J.; König, D.; Green, M. A.; Guillemoles, J. F., Slowing of carrier cooling in hot carrier solar cells. *Thin Solid Films* **2008,** 516, 6948.

15. Boukai, A. I.; Bunimovich, Y.; Tahir-Kheli, J.; Yu, J.-K.; Goddard, I., William A.; Heath, J. R., Silicon nanowires as efficient thermoelectric materials. *Nature* **2007,** 451, 168.

16. Yu, J.-K.; Mitrovic, S.; Tham, D.; Varghese, J.; Heath, J. R., Reduction of thermal conductivity in phononic nanomesh structures. *Nature Nanotechnology* **2010,** 5, 718.

Chapter 2: Device Fabrication and Surface Passivation

In this chapter, we provide detailed device fabrication protocols as well as surface passivation procedures. The surface recombination velocity was measured using microwave reflection photoconductivity decay, and the results are summarized below for each type of surface treatment. Parts of this and subsequent chapters are based on the author's published material.[1]

2.1 Device Fabrication

We utilized the superlattice nanowire pattern transfer (SNAP) technique[2-4] for the fabrication of nanowire (NWA) and nanohole array (NHA) devices. SNAP translates the film spacings within a molecular beam epitaxy-grown GaAs/$Al_xGa_{(1-x)}As$ superlattice structure into the width and pitch of nanowires of virtually any material that can be prepared in thin film form. Micrometer-scale contacts to the NWA (NHA) were patterned from the same single crystal material as the NWA (NHA) itself. Since SNAP is a nanowire patterning (rather than nanowire growth) approach, the starting thin film material may be precisely doped prior to NWA (NHA) formation, and side-by-side measurements of identically doped and treated NWAs (NHAs) and thin films are possible.

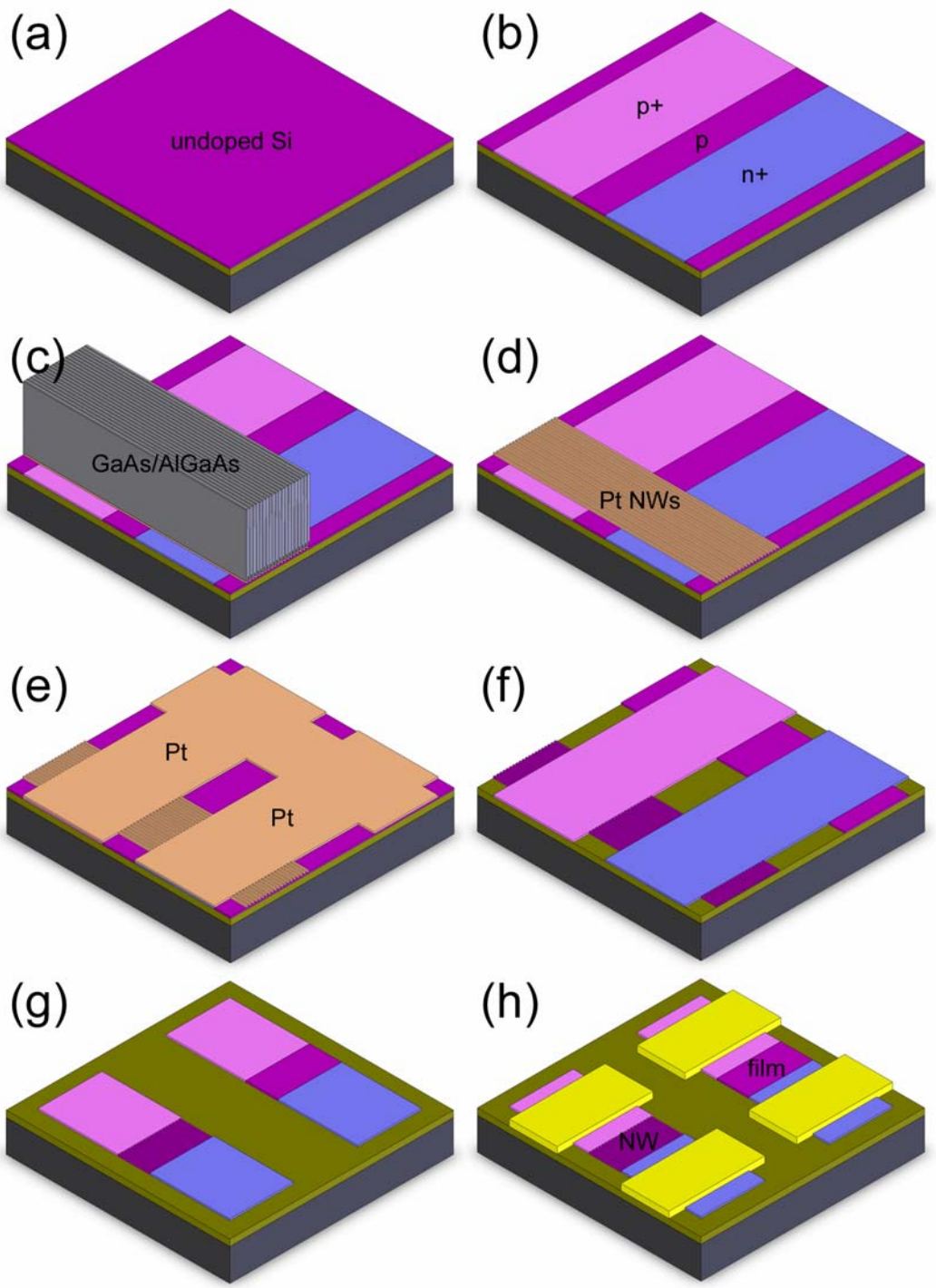

Figure 2-1. Schematic of fabrication steps for NWA devices.

2.1.1 Ion Implantation

The starting thin films were silicon-on-insulator (SOI) substrates (Soitec USA, Peabody, MA) comprised of 120 Å <100>-oriented single crystal Si epilayer atop 2000 Å buried SiO_2 (figure 2-1a). For the *pn*-junctions, two cycles of photolithographic masking and ion implantation (CORE Systems, Sunnyvale, CA) were performed to create heavily-doped *p*-type (dose of 3.8×10^{14} cm^{-2} B^+ at 2.5 keV) and *n*-type (dose of 3.2×10^{14} cm^{-2} P^+ at 6.5 keV) contact regions in the top silicon layer to promote the formation of ohmic contacts (figure 2-1b). A final low- or high-dose *p*-type implant without photoresist mask (dose of 3.8×10^{10} cm^{-2} B^+ or 3.8×10^{13} cm^{-2} B^+ at 2.5 keV) was performed to dope the device regions between the contacts. All implants were performed at an off-normal angle of 7° to mitigate implant profile broadening due to ion channeling.

2.1.2 Pre-activation Clean

The implanted SOI substrate was then subjected to a preactivation clean, modified from the standard RCA cleaning regimen. Our "modified RCA" recipe consists of a three-step procedure in solutions of H_2SO_4:H_2O_2 (3:1 v/v, 90 °C, 10 min), HF:H_2O (1:50 v/v, 15 s in dark), and H_2O:HCl:H_2O_2 (6:1:1 v/v, 80 °C, 10 min). The first step (piranha solution) removes surface organic contaminants, the second step (oxide strip) strips any native oxide off the silicon surface, while the final step (SC-2) removes metallic contaminants and regrows a chemical oxide. This recipe omits the standard organic clean (SC-1) based on solutions of H_2O:NH_4OH:H_2O_2, as we have found difficulty in controlling unintended etching of the ultrathin SOI during SC-1. Instead, we

have replaced the SC-1 step with the functionally similar piranha solution. After each step, the substrate was rinsed thoroughly with deionized water and dried with dry N_2.

2.1.3 Dopant Activation

After cleaning, the substrate was placed in a rapid thermal processor (RTP) and annealed under dry N_2 (900 °C for 10 s, ramp rate 35 K s^{-1}). After the anneal, the electrically active dopant concentration in the contact regions ranged between 0.6 and 2×10^{19} cm^{-3}, as determined from Hall probe measurements on test structures adjacent to the regions used for NWA and NHA patterning.

2.1.4 Superlattice Nanowire Pattern Transfer

Multiple devices were fabricated, and for each device, an array of silicon nanowires or nanoholes, aligned with the *pn*-junction, was formed using the SNAP technique.[2-4] To perform SNAP, superlattice wafers (IQE, Cardiff, U.K.) of alternating layers of GaAs/$Al_xGa_{(1-x)}As$ were cleaved into small pieces, and GaAs selectively etched away in NH_4OH:H_2O_2:H_2O (1:20:300 v/v) to expose a comb of parallel AlGaAs ridges running along the cleaved edge. Pt (100 Å) was evaporated at a 45° angle to coat just the tips of the ridges, forming an array of parallel Pt nanowires running along the edge. The superlattice chip was then placed array-side down onto the doped SOI substrate with a home-built aligner system (figure 2-1c), and held in place by a thin layer of thermally cured epoxy that had been previously spun onto the substrate. After curing, the entire assembly was placed gently in a H_2O_2:H_3PO_4:H_2O (1:5:50 v/v) solution to dissolve the GaAs/AlGaAs superlattice chip, leaving the array of Pt nanowires immobilized on the

substrate (figure 2-1d). A single round of SNAP patterning is sufficient for NWA devices; to produce NHA devices a second SNAP imprint is laid orthogonally across the first imprint and exactly aligned over the *pn*-junction. The second imprint is much more difficult to perform than the first, requiring angular and positional alignment accuracies on the order of ~0.1° and ~1 μm. Nevertheless, we routinely achieve this in our home-built aligner system.

2.1.5 Monolithic Contacts

Using a previously reported approach,[5] micrometer-size contacts to the nanostructures were established, using photolithographic patterning, from the same single crystal Si epilayer from which the nanostructures themselves were formed; thus, ohmic contacts can be made to the lightly doped NWA (NHA) via the heavily doped contacts. Thin film reference devices were also patterned adjacent to each NWA (NHA) device (figure 2-1e). A reactive-ion etch (RIE) step produced the NWA (NHA) and thin film devices and the associated contacts from the Si epilayer (figure 2-1f). Sectioning and isolation of the resulting devices was performed using standard photolithographic techniques (figure 2-1g).

2.1.6 Pre-oxidation Clean and Oxidation

The sectioned devices were cleaned once more with a preoxidation clean, and oxidized in a rapid thermal processor (RTP) under dry O_2 (1000 °C for 15 s, ramp rate 35 K s^{-1}) to grow a ~5 nm oxide surface layer. In early devices, the preoxidation clean was identical to the preactivation clean described above (the “modified RCA” recipe). In

later devices, it was found that better surface passivation could be obtained with a "HF-last RCA" recipe, where the order of the oxide strip and SC-2 steps was reversed (see following section for passivation quality results). Rapid thermal oxidation (RTO) has been similarly used to grow thin gate dielectrics;[6] here it is used to passivate the surfaces of photovoltaic devices. RTO provides higher quality surface passivation than can be achieved with native or chemical oxides[7] and is crucial for good photovoltaic performance.[8] With later devices, we also experimented with postoxidation annealing (POA) under Ar (1000 °C for 3 min, ramp rate 35 K s^{-1}). POA serves to densify the RTO oxide and reduce oxide fixed charge,[9, 10] resulting in improved surface passivation. Further improvement of the oxide quality was achieved with a subsequent forming gas anneal (FGA, 5% H_2 in N_2) with the RTP (475 °C for 5 min).[11-14] We were able to achieve good device performance by following this passivation protocol; otherwise, our devices rarely exhibited photovoltaic behavior. Nonetheless, we believe that our best devices are still limited by surface recombination and that their performance can be further improved by optimizing the surface passivation layer.

2.1.7 Contact Metallization

Finally, standard photolithographic and metal deposition techniques were used to define metal contacts to the devices (figure 2-1h). In early devices using the modified RCA preoxidation clean, a short dip in dilute BOE:H_2O (1:25 v/v, 10 s in dark) was sufficient to remove oxides over the contact regions; later devices using the HF-last recipe had denser, higher-quality oxide passivation and required a longer etch time in more concentrated BOE:H_2O (1:10 v/v, ~30 s in dark). After oxide removal over the

contact regions, Ti/Pt/Au (100/100/1200 Å) contacts were evaporated onto the devices in an e-beam evaporator (CHA Industries, Fremont, CA). The final metal liftoff procedure was performed just before measurement to minimize device degradation from extended exposure to ambient air. After liftoff, further improvements in performance could be obtained from a postmetallization anneal (PMA) under forming gas (5% H_2 in N_2) in the RTP (350 °C for 30 min) to reduce e-beam metallization-induced defects.[11, 12, 15-18] The Ti/Pt/Au contacts appear to be stable as long as the annealing temperature does not exceed the Au-Si eutectic temperature of 363 °C,[19] and samples which have undergone even four cycles of PMA have not shown appreciable degradation.

2.2 Surface Recombination Velocity Measurements

2.2.1 Oxidation Protocol

To quantify the surface passivation quality obtainable from our oxidation treatments, we performed surface recombination velocity (SRV) measurements on test wafers subjected to various permutations of our passivation protocol. Double-side polished, 4" diameter, 412 ± 1 μm thick, intrinsic float-zone silicon wafers (Virginia Semiconductor) were diced into approximately 1" square pieces, taking care not to scratch or mar the polished surfaces. Each of the wafer pieces was dipped in dilute HF:H_2O (1:50 v/v, ~10 s) to strip off the native oxide, rinsed with deionized water and dried, and then subjected to either the modified RCA clean or the HF-last recipe. Following the preoxidation clean, the pieces were then loaded into the RTP for RTO processing in dry O_2, using a specially prepared carrier wafer with a 1" diameter hole cut out in its center. Loading the wafer piece over the hole allows both sides of the sample to

be oxidized equally and simultaneously. After oxidation, some pieces also underwent additional POA in inert Ar gas. Finally, all pieces were FGA treated before the SRV was measured.

2.2.2 Surface Recombination Velocity Measurement

SRV measurements were performed in a microwave reflection photoconductance decay (MW-PCD) apparatus (see figure 2-2). Samples were placed in a covered Petri dish and an infrared pulse from a diode laser shone on the sample. During the duration of the laser pulse, light is absorbed within the sample bulk and creates a large number $\Delta n(0)$ of electron-hole pairs, which changes the sample conductivity $\sigma = q(\mu_n n + \mu_p p)$ and is monitored using its microwave reflectivity as a function of time. As the electron-hole pairs recombine, the conductivity is restored to a low value typical of the intrinsic silicon and the microwave reflectivity decays. The reflected microwave signal is therefore a direct probe of the number of free carriers $\Delta n(t)$ within the sample, and its decay time is a measure of the carrier recombination rate. Microwave reflectivity decay curves were collected on a digital oscilloscope synchronized with the infrared laser pulses, and hundreds of individual curves were averaged together during the course of each ~1 min acquisition. The intensity of the laser pulses was set such that all samples were in low injection during the measurements.

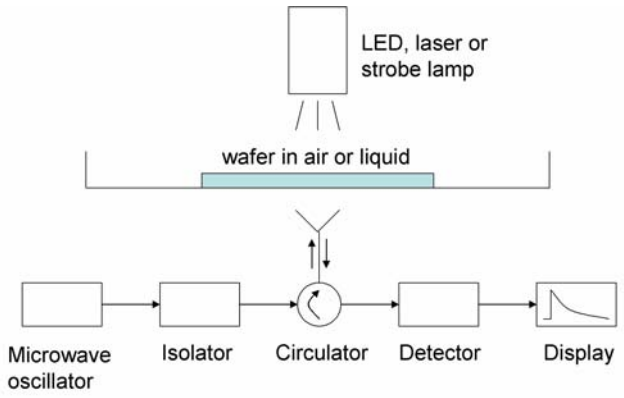

Figure 2-2. Schematic of microwave reflection photoconductance decay (MW-PCD) apparatus.

2.2.3 Data Analysis

We found that all the decay curves could be fitted with a single exponential $\Delta n(t) = \Delta n(0)\exp(-t/\tau_{eff})$ if the initial transient of the decay was ignored, yielding an effective minority carrier lifetime τ_{eff} for each type of surface treatment that was investigated (Figure 2-3). Following Schroder,[20] the effective recombination rate at low injection $1/\tau_{eff} = 1/\tau_B + 1/\tau_S$ has contributions from the bulk recombination rate $1/\tau_B$ (a function of the quality of the bulk material) as well as the surface recombination rate $1/\tau_S = D\beta^2$. By assuming that all the recombination is occurring at the sample surfaces and ignoring bulk recombination ($1/\tau_B = 0$), one can obtain an upper estimate for the SRV. Here we have written the surface recombination term as a product of the minority carrier diffusion constant at low injection *D*, and the square of a parameter β determined by the transcendental equation $\tan(\beta d/2) = s_r/\beta D$ where *d* is the wafer thickness and s_r is the SRV.

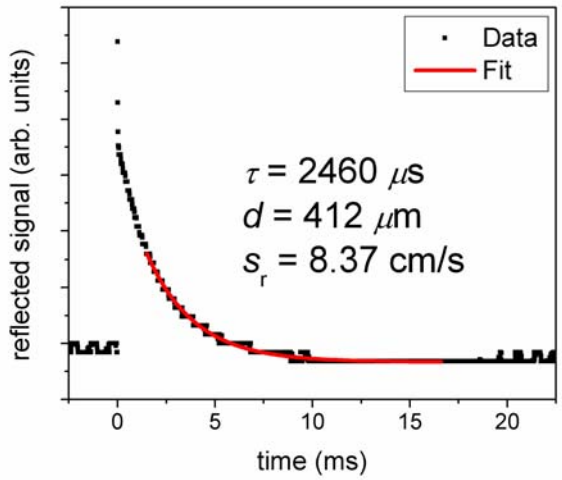

Figure 2-3. A typical decay curve and its exponential fit.

There are two important limiting cases for this transcendental equation. When the SRV is small, $\tau_S(s_r \to 0) = d/2s_r$ and the SRV can be estimated directly from the effective lifetime with $s_r \le d/2\tau_{eff}$. When the SRV is large, $\tau_S(s_r \to \infty) = d^2/\pi^2 D$ and surface recombination is so fast that the effective surface recombination rate $1/\tau_S$ is limited by minority carrier diffusion to the surfaces. For our wafer pieces, assuming a typical value for silicon of $D \approx 20 - 30$ cm^2 s^{-1}, we obtain $\tau_S(s_r \to \infty) \approx 6 - 9$ μs. Once the measured effective lifetime approaches this value, the estimated SRV is "large" and should now be considered a *lower* estimate of surface recombination in a diffusion-limited regime. Our SRV estimates, averaged from multiple locations on each sample, are summarized in table 2-1. Where noted, oxide thicknesses were measured immediately after the oxidation with a single wavelength ellipsometer at 632.8 nm (Gaertner), using an optical model consisting of a layer of silicon dioxide atop a silicon substrate.

2.2.4 Results

Effective lifetimes from the as-received native oxide and the acid passivated samples are limiting examples of respectively poor and excellent passivation. All of our passivation protocols result in SRVs that lie in between these bounds. Without any oxidation treatment, a chemical oxide formed after modified RCA cleaning has unremarkable passivation performance with SRV = 1300 cm s^{-1}. Even after a short 15 s RTO treatment followed by 5 min of FGA, the oxide is not improved significantly, and a 3 min POA is required to densify the oxide before SRVs of 80 cm s^{-1} can be achieved.

Table 2-1. Effective minority carrier lifetimes and surface recombination velocities for various surface passivation treatments on silicon wafers.

Protocol	τ_{eff} (μs)	s_r (cm s^{-1})	Notes
As-received native oxide	9.9	>2100	Diffusion-limited.
Piranha + HF etch, under H_2SO_4	3900	5.3	No oxide. Acid passivated.
Modified RCA followed by:			
No further treatment	16	1300	20 Å. Chemical oxide.
15” RTO + FGA	19	1100	28 Å. NWAs, early NHAs.
15” RTO + POA + FGA	250	80	31 Å.
HF etch + 2’ RTO + POA + FGA	1200	17	77 Å.
	1700	12	100 Å.
	1700	12	131 Å.
HF etch + 45” RTO + POA + FGA	1500	14	64 Å.
HF-last RCA followed by:			
2’ RTO + POA + FGA	1200	17	
	1600	13	
45” RTO + POA + FGA	2500	8.3	65 Å. Similar to late NHAs.

In the abovementioned samples, the chemical oxide remains on the sample before RTO, potentially introducing contaminants from the cleaning reagents during high-temperature annealing. Therefore, we decided to try removing the chemical oxide formed after RCA cleaning with a brief etch in dilute HF:H_2O (1:50 v/v, 15 s in dark) before submitting the sample to RTO. The resulting samples have greatly improved SRVs between 12 and 17 cm s^{-1}, with no apparent dependence on oxide thickness. These samples have seen two separate dilute HF etches: the first during the modified RCA clean, and the second during the chemical oxide removal step. We wanted to know if the first HF etch was crucial for obtaining low SRV passivation, and thus excluded this step during the processing of the remaining wafers. These are the "HF-last RCA" samples and we do not observe any perceptible difference in the passivation quality.

As can be seen, a HF etch performed just before RTO yields a greatly increased minority carrier lifetime, with SRV of <10 cm s^{-1} possible although values around 10 – 20 cm s^{-1} are more routinely achieved. These are among the best SRVs ever achieved for silicon,[21-26] and indicate that the surface passivation we can obtain from our ultrathin oxides can rival traditional thermal oxides prepared by slow furnace oxidation.

2.3 Summary

We have described the fabrication procedures we use to produce our nanowire and nanohole array devices. Using microwave reflection photoconductance decay measurements, we evaluated the passivation performance of a variety of oxidation protocols. The best performance is obtained when a dilute hydrofluoric acid etch is used to remove the chemical oxide grown during preoxidation cleaning, before the sample is

introduced into the oxide growth chamber. Furthermore, the use of postoxidation anneals under inert atmosphere followed by forming gas annealing serves to densify the oxide, removes oxide charge and reduces surface recombination. The best performance was obtained by combining these ideas and produced ultrathin passivating oxides that exhibited surface recombination velocities routinely below 20 cm s^{-1}.

2.4 References

1. Tham, D.; Heath, J. R., Ultradense, deep subwavelength nanowire array photovoltaics as engineered optical thin films. *Nano Letters* **2010,** 10, 4429.

2. Melosh, N. A.; Boukai, A.; Diana, F.; Gerardot, B.; Badolato, A.; Petroff, P. M.; Heath, J. R., Ultrahigh-density nanowire lattices and circuits. *Science* **2003,** 300, 112.

3. Wang, D.; Sheriff, B. A.; Heath, J. R., Silicon p-FETs from ultrahigh density nanowire arrays. *Nano Letters* **2006,** 6, 1096.

4. Heath, J. R., Superlattice nanowire pattern transfer (SNAP). *Accounts of Chemical Research* **2008,** 41, 1609.

5. Wang, D.; Bunimovich, Y.; Boukai, A.; Heath, J. R., Two-dimensional single-crystal nanowire arrays. *Small* **2007,** 3, 2043.

6. Green, M. L.; Gusev, E. P.; Degraeve, R.; Garfunkel, E. L., Ultrathin (<4 nm) SiO_2 and Si-O-N gate dielectric layers for silicon microelectronics: Understanding the processing, structure, and physical and electrical limits. *Journal of Applied Physics* **2001,** 90, 2057.

7. Petrova-Koch, V.; Muschik, T.; Kux, A.; Meyer, B. K.; Koch, F.; Lehmann, V., Rapid-thermal-oxidized porous Si - The superior photoluminescent Si. *Applied Physics Letters* **1992,** 61, 943.

8. Aberle, A. G., Surface passivation of crystalline silicon solar cells: A review. *Progress in Photovoltaics: Research and Applications* **2000,** 8, 473.

9. Poindexter, E. H.; Caplan, P. J.; Deal, B. E.; Razouk, R. R., Interface states and electron spin resonance centers in thermally oxidized (111) and (100) silicon wafers. *Journal of Applied Physics* **1981,** 52, 879.

10. Balk, P.; Aslam, M.; Young, D. R., High temperature annealing behavior of electron traps in thermal SiO_2. *Solid State Electronics* **1984,** 27, 709.

11. Balk, P.; Klein, N., Generation of interface states in MOS systems. *Thin Solid Films* **1982,** 89, 329.

12. Poindexter, E. H.; Caplan, P. J., Electron spin resonance of inherent and process induced defects near the Si/SiO_2 interface of oxidized silicon wafers. *Journal of Vacuum Science and Technology A* **1988,** 6, 1352.

13. Fukuda, H.; Ueno, T.; Kawarada, H.; Ohdomari, I., Effect of deuterium anneal on SiO_2/Si(100) interface traps and electron spin resonance signals of ultrathin SiO_2 films. *Japanese Journal of Applied Physics* **1993,** 32, L569.

14. Stathis, J. H.; Buchanan, D. A.; Quinlan, D. L.; Parsons, A. H., Interface defects of ultrathin rapid-thermal oxide on silicon *Applied Physics Letters* **1993,** 62, 2682.

15. Lee, H.-S., Metal-oxide-semiconductor instability produced by electron-beam evaporation of aluminum gates. *IEEE Transactions on Electron Devices* **1978,** ED-25, 795.

16. Ning, T. H., Electron trapping in SiO_2 due to electron-beam deposition of aluminum. *Journal of Applied Physics* **1978,** 49, 4077.

17. Peckerar, M.; Fulton, R.; Blaise, P.; Brown, D.; Whitlock, R., Radiation effects in MOS devices caused by x-ray and e-beam lithography. *Journal of Vacuum Science and Technology* **1980,** 16, 1658.

18. Chen, J. Y.; Henderson, R. C.; Martin, R.; Patterson, D. O., Enhanced radiation effects on submicron narrow-channel NMOS. *IEEE Transactions on Nuclear Science* **1982,** NS-29, 1681.

19. Kanamori, S., A study on the penetration of platinum into silicon in Ti/Pt/Au beam lead metallization systems. *Thin Solid Films* **1981,** 75, 19.

20. Schroder, D. K., *Semiconductor Material and Device Characterization*. 2nd ed.; John Wiley & Sons: New York, 1998.

21. Yablonovitch, E.; Allara, D. L.; Chang, C. C.; Gmitter, T.; Bright, T. B., Unusually low surface-recombination velocity on silicon and germanium surfaces. *Physical Review Letters* **1986,** 57, 249.

22. Stephens, A. W.; Green, M. A., Effectiveness of 0.08 molar iodine in ethanol solution as a means of chemical surface passivation for photoconductance decay measurements. *Solar Energy Materials and Solar Cells* **1997,** 45, 255.

23. Takato, H.; Sakata, I.; Shimokawa, R., Surface passivation effect of silicon substrates due to quinhydrone/ethanol treatment. *Japanese Journal of Applied Physics* **2001,** 40, L1003.

24. Kerr, M. J.; Cuevas, A., Very low bulk and surface recombination in oxidized silicon wafers. *Semiconductor Science and Technology* **2002,** 17, 35.

25. Michalak, D. J.; Gstrein, F.; Lewis, N. S., The role of band bending in affecting the surface recombination velocities for Si(111) in contact with aqueous acidic electrolytes. *Journal of Physical Chemistry C* **2008,** 112, 5911.

26. Koyama, K.; Ohdaira, K.; Matsumura, H., Extremely low surface recombination velocities on crystalline silicon wafers realized by catalytic chemical vapor deposited SiN_x/a-Si stacked passivation layers. *Applied Physics Letters* **2010,** 97, 082108.

Chapter 3: Device Characterization Techniques

In this chapter, we describe various techniques used to characterize the device structure and morphology. Using optical and electron microscopy and ellipsometry, we determine the structural parameters for an optical model of our devices that is used in chapter 4. Minority carrier diffusion lengths were also measured using scanning photocurrent imaging, enabling a direct estimate of the active area of the device.

3.1 Optical Microscopy

When fabricated devices were imaged optically, high quality samples always appeared homogeneous under bright- and dark-field microscopy, exhibiting a uniform coloration over the extent of the device. Devices with poor periodicity or defects often appeared mottled, with streaks of slightly different shades running through the device. As shown in figure 3-1, both nanowire arrays (NWA) and nanohole arrays (NHA) appear dark pink under optical microscopy, with distinct coloration differences from the surrounding contacts (bright pink) and the underlying oxide (olive green).

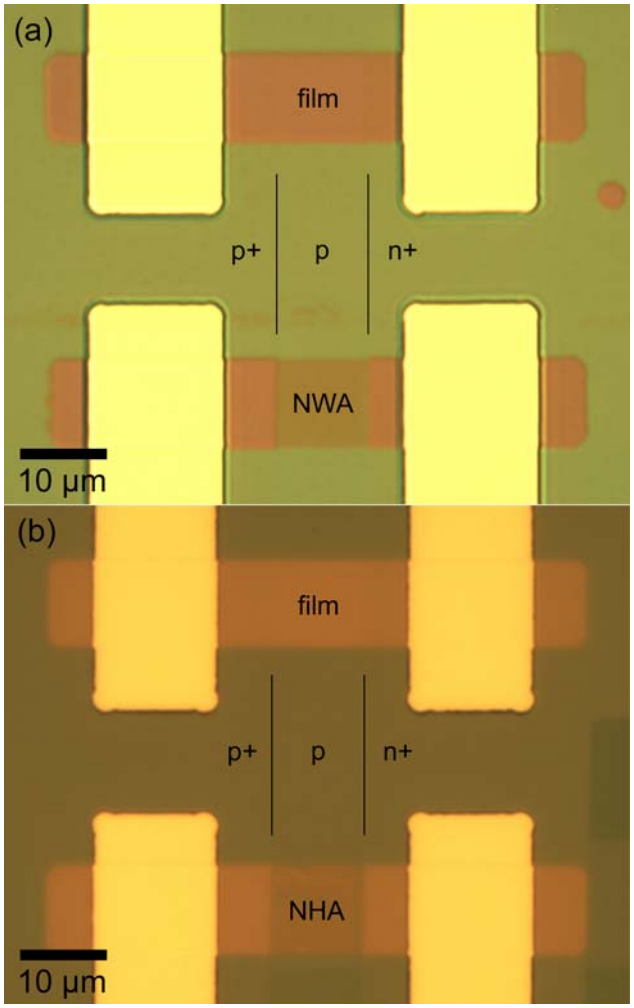

Figure 3-1. Optical micrographs of nanowire array device and nanohole array device.

3.2 Scanning Electron Microscopy

We characterized the morphology of our nanostructure arrays using scanning electron microscopy (SEM). Plan-view images of the arrays were obtained at 30 kV in a XL30 FEG SEM. Samples that appeared most homogeneous from light microscopy always exhibited high structural perfection, with the array periodicity extending over the entire device area. The SEM micrographs confirm that the best arrays are of high quality and well ordered. In the NWA device shown here (figure 3-2a), nanowires are

continuous, straight and well delineated with clean sidewalls over their entire lengths. In this device, individual nanowires are nominally 10 μm long, 10 nm thick, 20 nm wide, and separated by 14 nm from adjacent nanowires. The NHA device shown in figure 3-2b has regularly spaced, nearly identically sized holes over the entire device, with occasional local defects such as missing or merged holes. Individual nanoholes are nominally 12 nm wide, separated by 20 nm from each other, and are arranged on a 32 nm pitch square lattice over the entire extent of the 10×10 μm^2 device.

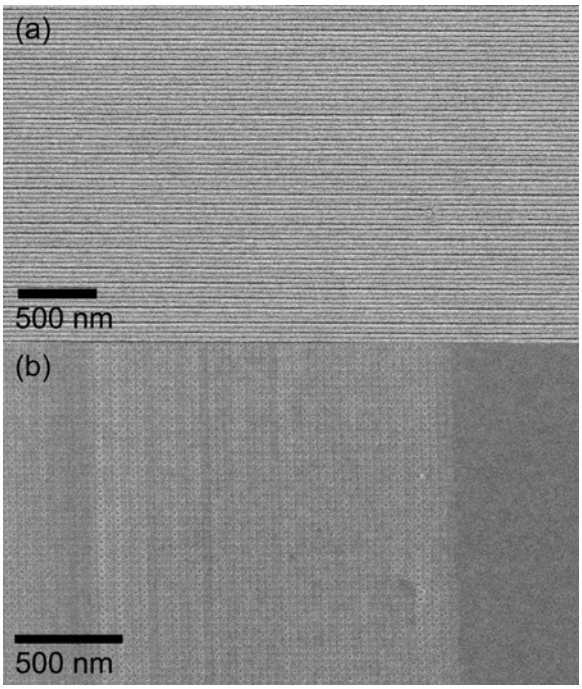

Figure 3-2. Scanning electron micrographs of nanowire array and nanohole array devices.

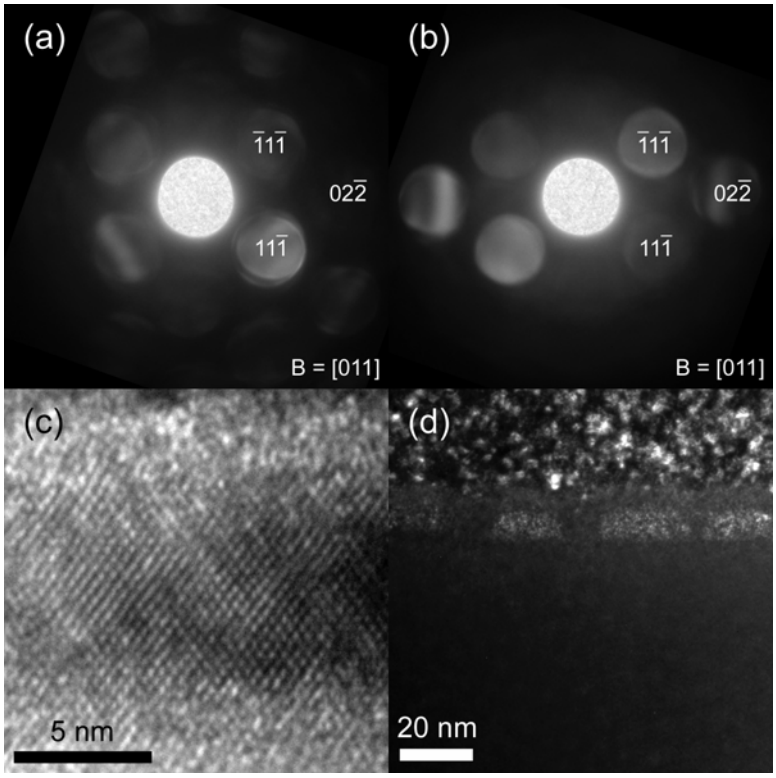

Figure 3-3. Convergent beam electron diffraction patterns of bulk film and nanowire devices, taken along the B = [011] zone (parallel to the nanowire axis).

3.3 Cross-sectional Transmission Electron Microscopy

To image the sidewall profiles of the arrays, we turned to cross-sectional transmission electron microscopy. Cross sections of the nanowire arrays were prepared using the focused-ion beam (FIB) lift-out technique[1, 2] in a Nova 600 DualBeam FIB/SEM (FEI Company, Hillsboro, OR) equipped with an Autoprobe 200 micromanipulator system (Omniprobe, Dallas, TX). Initial cuts were made at a higher ion energy of 30 kV and high beam currents of >1000 pA for increased speed. Final thinning to electron transparency was performed with ions at 10 kV at glancing incidence and lower beam currents of <100 pA to minimize sample damage.

After the cross section was prepared, it was loaded into a Tecnai TF20ST TEM (FEI Company, Hillsboro, OR) for imaging at 200 kV. Sometimes, the cross-sectional sample was too thick, and contained contrast contributions from inelastically scattered transmitted electrons. In that case, a Gatan Imaging Filter (Gatan, Pleasanton, CA) was used to image the zero-loss electrons and provided improved contrast. Convergent beam electron diffraction (CBED) was performed by focusing the beam to crossover over the device regions and capturing the diffraction patterns on a charge-coupled device at the camera plane (figure 3-3a,b). With sufficiently thin sample regions, high-resolution transmission electron micrographs were acquired along the [011] zone of the sample and confirm that the high crystallinity of the devices are retained after processing (figure 3-3c). By placing an objective aperture about the $(\bar{1}1\bar{1})$ spot, tilted-beam dark-field micrographs also show that the NWA devices remain crystalline (figure 3-3d).

Cross-sectional TEM indicates that both the NWA and thin film devices retain the crystallinity of the starting SOI wafer after processing. For the film device (figure 3-4a), TEM measurements suggest an optical model of 5.4 nm SiO_2 / 9.5 nm Si / 200 nm of SiO_2, which agrees well with the spectroscopic ellipsometry estimates of 5.41 nm SiO_2 / 9.22 nm Si / 201.72 nm SiO_2 (see following section). The ellipsometry measurements were used to model the film device in RCWA. TEM micrographs of the NWA device (figure 3-4b) show a corrugated ridgelike texture: 20 nm wide, 9 nm tall nanowires, spaced 12 nm apart, with 10 nm deep overetch pits in the underlying oxide. Each nanowire is surrounded by a 5 nm oxide sheath, and nanowire sidewalls are rounded due to high-temperature oxidation.

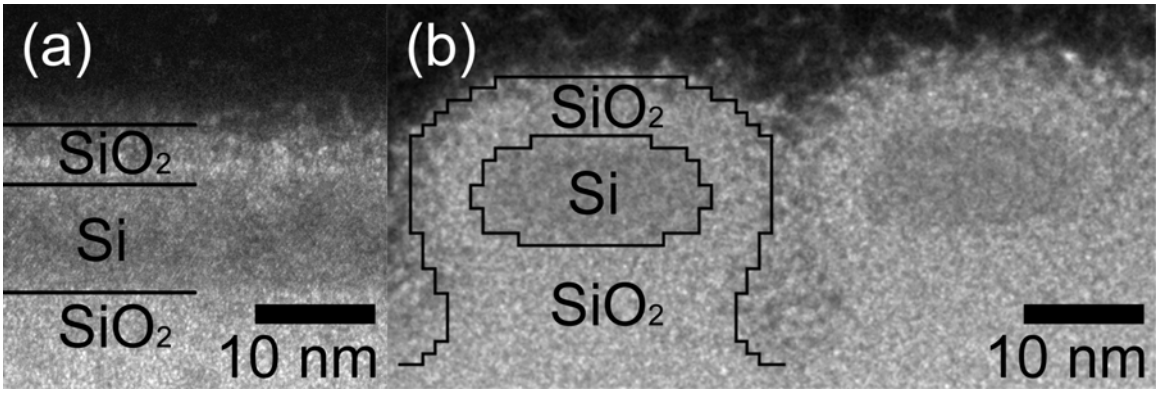

Figure 3-4. Cross-sectional transmission electron micrographs of thin film device and nanowire array device.

3.4 Spectroscopic Ellipsometry

To characterize the optical properties of the film devices, spectroscopic ellipsometry (SE) was performed on 2×2 mm^2 areas of bulk film regions of the chip using a SE850 UV/Vis spectroscopic ellipsometer equipped with microspot focusing objectives (Sentech Instruments GmbH, Berlin, Germany). These objectives enable measurement of the ellipsometric angles Δ and Ψ from regions only a few hundred microns in size. The ellipsometric constants were measured between 300 and 820 nm at an incidence of 70° and fitted for layer thicknesses with a model where incident light passes through air onto a three-layer thin film SiO_2/Si/SiO_2 atop a Si substrate. We used literature values for the refractive indices of silicon[3, 4] and silicon dioxide.[5, 6]

3.5 Spectroscopic Imaging Ellipsometry

Because the large bulk film regions of the chip are far from the actual device regions, the thickness estimates obtained from conventional spectroscopic ellipsometry can be significantly different from the actual layer thicknesses. To determine the layer

thicknesses more accurately, spectroscopic imaging ellipsometry (SIE) was performed on the film devices that were fabricated adjacent to the nanostructured devices. These measurements were made on 4×4 μm^2 regions in the middle of each film device between 366 and 1002 nm at incidence angles of 40°, 50°, and 60°, using a Nanofilm EP3 spectroscopic imaging ellipsometer (Accurion GmbH, Goettingen, Germany). The layer thicknesses were once again fitted using the three-layer thin film model described above, using literature values for the refractive indices.

The resulting SE and SIE data fits are summarized for representative samples in table 3-1 below.

Table 3-1. Fitted layer thicknesses for spectroscopic ellipsometry and spectroscopic imaging ellipsometry data for several samples.

	SE fits (nm)	SIE fits (nm)	
Sample	**SiO_2 / Si / SiO_2**	**SiO_2 / Si / SiO_2**	**Notes**
NWA1	5.41 / 9.22 / 201.72	-	Nanowire array.
NHA1	4.05 / 9.14 / 202.42	-	Disordered nanohole array.
NHA2	4.07 / 9.31 / 202.53	5.93 / 9.28 / 200.24	Disordered nanohole array.
NHA3	5.72 / 8.67 / 200.25	9.04 / 7.83 / 200.84	Ordered nanohole array.

3.6 Minority Carrier Diffusion Length

3.6.1 Scanning Photocurrent Imaging

Minority carrier diffusion lengths were measured using a WITec AlphaSNOM (WITec Wissenschaftliche Instrumente und Technologie GmbH, Ulm, Germany) scanning near-field optical microscope (SNOM). Light from laser diodes at 405 nm

(blue) or 650 nm (red) was chopped at 83 Hz and fiber-coupled into the microscope. An objective lens was used to focus the laser light onto the device (far-field illumination), or onto the 100 nm aperture of a SNOM tip (near-field illumination). The device was mounted on a computer controlled stage under the objective lens, connected to a SR570 current-to-voltage preamplifier and the preamplifier output voltage measured with a SR830 lock-in amplifier (Stanford Research Systems, Sunnyvale, CA). To acquire the scanning photocurrent images, the laser probe beam was rastered across the device while recording the lock-in output as a function of probe position. During the measurement, the devices were weakly illuminated using the microscope lamp to remove artifacts arising from light absorption in the substrate wafer. The minimum illumination level was used to remove capacitance transients from the output photocurrent so as to obtain a square wave output.

Scanning photocurrent images acquired with far-field illumination were resolution limited by the quality of the focusing objective or by focusing errors. In figure 3-5, we have overlaid the scanning photocurrent images obtained at red and blue wavelengths in their respective colors on the grayscale optical micrograph. The excellent overlap between the red and blue photocurrent images indicates that there is no wavelength dependence for the minority carrier diffusion length. There is some spurious intensity in both blue and red photocurrent images even in regions far away from the junction due to beam reflections and a poorly focused probe beam.

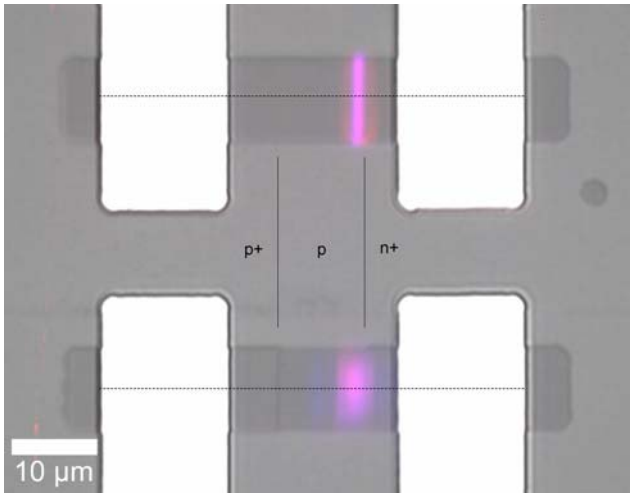

Figure 3-5. Optical micrograph of bulk film and nanowire array devices, overlaid with far-field scanning photocurrent images.

3.6.2 Scanning Near-Field Optical Microscopy

On the other hand, near-field illumination using the SNOM tip in contact-mode enabled high-resolution measurements of the diffusion length limited only by the tip aperture size (figure 3-6). Unfortunately, because the tip is dragged across the surface, the sample undergoes damage during the measurement and can typically only tolerate a few repeat measurements. After the measurement, line profiles were taken along the device axis and fitted to an exponential function to determine the diffusion lengths on either side of the junction. An exponential fit on the left (right) side of the peak yields the minority carrier diffusion length L_e (L_h), with measurement resolution determined by the finite size of the SNOM tip aperture (100 nm). This yields upper estimates for the total diffusion length L_{max} ~ 400 and 300 nm respectively for the bulk film and nanowire array devices. Accounting for the broadening due to the tip aperture, the respective lower estimates are L_{min} ~ 200 and 100 nm.

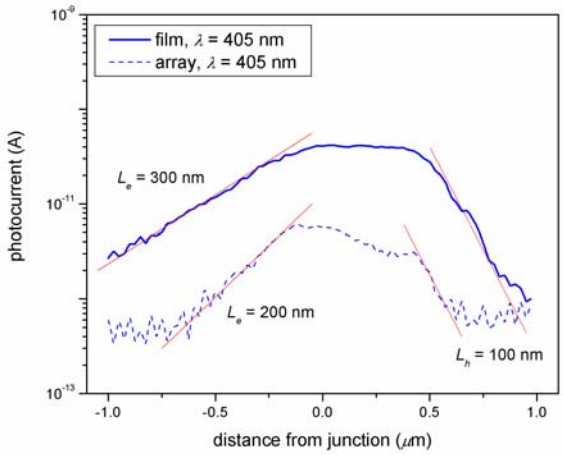

Figure 3-6. Line profiles through near-field scanning photocurrent images obtained with a scanning near-field optical microscope in contact mode, taken along the dashed lines in Figure 3-5.

3.7 Summary

We have described the techniques we use to characterize the structural and parameters of our nanostructure arrays. Direct imaging of the fabricated structures using optical microscopy and scanning electron microscopy shows that the best structures are highly periodic and exhibit a high degree of structural perfection throughout the extent of the device. Cross-sectional transmission electron microscopy enables direct visualization of the vertical profiles and morphology of the device, which will be used to develop an optical model of these materials in chapter 4. Indirect characterization techniques such as spectroscopic ellipsometry and spectroscopic imaging ellipsometry provide similar estimates for layer thicknesses as direct cross-sectional imaging. This provides confidence in their accuracy and allows us to rely on the faster indirect approaches to obtain layer thickness information. Scanning photocurrent imaging confirms that these devices are well-behaved diodes with their photoactive regions exactly in the designed location. With a scanning near-field optical microscope, high-resolution scanning

photocurrent imaging was used to obtain direct estimates of the minority carrier diffusion lengths, which is used in chapter 5 to analyze the photovoltaic performance of these materials.

3.8 References

1. Giannuzzi, L. A.; Stevie, F. A., A review of focused ion beam milling techniques for TEM specimen preparation. *Micron* **1999,** 30, 197-204.

2. Tham, D.; Nam, C.-Y.; Fischer, J. E., Microstructure and composition of focused-ion-beam-deposited Pt contacts to GaN nanowires. *Advanced Materials* **2006,** 18, 290.

3. Aspnes, D. E.; Studna, A. A., Dielectric functions and optical parameters of Si, Ge, GaP, GaAs, GaSb, InP, InAs, and InSb from 1.5 to 6.0eV. *Physical Review B* **1983,** 27, 985.

4. Edwards, D. F., Silicon (Si). In *Handbook of Optical Constants of Solids*, Palik, E. D., Ed. Academic Press: New York, 1985; p 547.

5. Malitson, I. H., Interspecimen comparison of the refractive index of fused silica. *Journal of the Optical Society of America* **1965,** 55, 1205.

6. Philipp, H. R., Silicon dioxide (SiO_2) (Glass). In *Handbook of Optical Constants of Solids*, Palik, E. D., Ed. Academic Press: New York, 1985.

Chapter 4: Optical Modeling of Devices

In this chapter, we describe the optical models that are used to calculate the absorptance of the nanowire and nanohole array devices. We begin with the rigorous coupled-wave analysis (RCWA) that solves exactly Maxwell's equations for periodic structures. These calculations were performed for nanowire and nanohole array devices, by entering the optical models gleaned from the structural studies in chapter 3 into readily available one- and two-dimensional RCWA codes. The results indicate that these deep subwavelength nanowire and nanohole arrays behave as homogeneous optical materials, motivating a search for a computationally inexpensive effective medium approximation for our devices.

4.1 Rigorous Coupled-Wave Analysis Calculations

The rigorous coupled-wave analysis (RCWA) represents periodic surface features as a Fourier series and propagates the incident wave through the optical model by solving Maxwell's equations exactly. Essentially, a three-dimensional grid is overlaid over a unit cell of the periodic structure, and the optical model is built up layer by layer by assigning appropriate optical constants to each volume element. In each layer, the periodic pattern of optical constants is assumed to be constant throughout the entire layer thickness and is approximated as a truncated Fourier series. The illumination conditions are then defined

and the differential equations solved layer by layer as the incident wave enters the structure from the superstrate and exits via the substrate. Special care is taken to match the electromagnetic boundary conditions at each interface. In this way, the reflected and transmitted diffraction amplitudes are obtained for the entire multilayer structure, from which the reflectance and transmittance can be calculated for any given diffracted order. The reflectance is evaluated at the upper interface between the superstrate and the topmost layer, while the transmittance is evaluated at the lower interface between the bottommost layer and the substrate.

4.2 Absorptance Calculations for Nanowire Arrays

We calculated the optical properties of the film and NWA devices using an open-source implementation[1] of Moharam's formulation[2] of the rigorous coupled wave analysis (RCWA). RCWA is ideally suited for periodic structures and is commonly utilized for calculations of reflectance R and transmittance T.[3-5] We used it to calculate the absorptance $A = 1 - R - T - S$, assuming no light scattering ($S = 0$). This assumption is valid for materials that are homogeneous on the length scale of the incident radiation. The NWA device features are well-ordered and deep in the subwavelength regime and so this approximation is excellent, as we shall demonstrate later.

To generate an optical model for the nanowire array, we overlaid a square mesh over the TEM image (figure 3-4b) and assigned phases (air, Si or SiO_2) to each 1×1 nm^2 grid square. A single period of the resulting model is illustrated in figure 3-4b, with the total thickness of the underlying oxide set to 202 nm. In our limited experience, the RCWA results are only weakly affected by changes in shape, and more strongly impacted

by changes in periodicity. The exact choice of the model morphology and mesh resolution is relatively unimportant, so long as the array period and nanowire size is well characterized.

There is no general restriction on the grid resolution, uniformity or geometry, so we have used a somewhat coarse (1 nm × 1 nm) uniform square grid to discretize the nanowire array for speed and simplicity. The superstrate (air or vacuum) and substrate (680 μm thick silicon handle wafer) media are assumed to be continuous, isotropic and infinite. For a grating structure like our nanowire arrays (NWAs) with features dependent on the x,y,z-space coordinates, the Fourier series is one-dimensional in x (normal to the nanowires). In the y-direction (parallel to the nanowire axis) the features are assumed to be infinite in extent, which is a reasonable approximation given that our arrays are ≥10 μm long, more than 10 times longer than the wavelengths of interest. In the z-direction, we used 3 layers to represent the bulk film device (see figure 3-4a) and 17 layers to represent the nanowire array structure (figure 3-4b). A total of 65 Fourier modes were included in the calculation assuming normal incidence plane-wave illumination. To calculate the absorptance $A = 1 - R - T - S$, we used the zero-order (specular) reflectance R_0 and transmittance T_0 and assume no scattering ($S = 0$). We have verified that the reflectance and transmittance are identically zero for nonzero diffraction orders; this implies complete absorption and therefore evanescent diffracted waves for higher orders.

The calculation was performed on the optical model described in the inset of figure 4-1, between 200 and 825 nm, using normal incidence illumination. As is common in the field of grating physics, we have defined the plane of incidence to be perpendicular to the nanowire axis, so that TE- (TM-) polarized waves have electric field components

parallel (perpendicular) to the nanowires. Each calculation took several minutes on a standard personal computer, yielding results with accuracy on the order of 10^{-4}, typical for RCWA.[6] Finally, the RCWA results were convolved with the measured monochromator slit function. To obtain the absorptance of the NWA for any arbitrary polarization, we assume that the illumination is incoherent, and calculated the weighted average of the absorptances for TE- and TM-polarizations. We did not correct for the polarization bias as the effect is small in our system and does not affect the results appreciably.

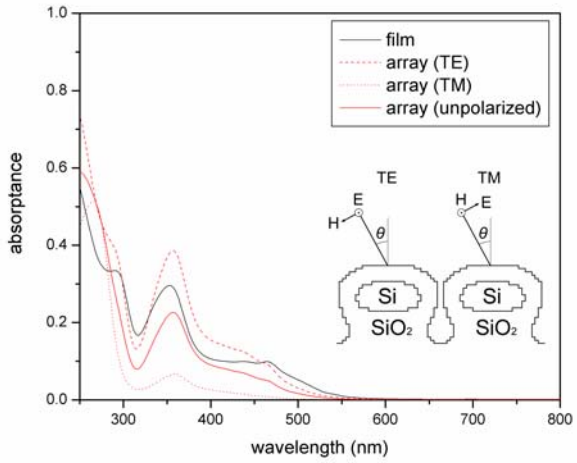

Figure 4-1. Calculated absorptances for nanowire array.

Figure 4-1 shows the absorptance for the film and NWAs, calculated using RCWA for collimated illumination at normal incidence (see inset for the illumination geometry). The spectra show strong oscillatory features due to thin-film interference effects. RCWA predicts no polarization dependence for the film absorptance, as expected for an optically isotropic material like silicon. On the other hand, the NWA devices are predicted to exhibit pronounced polarization effects in the absorptance for TE- (electric

field parallel to nanowires) and TM-polarized (magnetic field parallel to nanowires) light. Absorption of TE-polarized light is enhanced substantially over that of the film over most wavelengths, while TM-polarized light is hardly absorbed except for the shortest wavelengths. As the individual nanowires are 20 nm in width and far smaller than the illumination wavelengths, all diffracted waves are evanescent except for the specular zero-order reflection. We have examined the calculation results and find no far-field reflected or transmitted diffraction intensity at all higher orders. Therefore, the NWA behaves like a homogeneous bulk material with anisotropic refractive indices down to the shortest wavelengths. That is, it exhibits birefringence. This is distinctly different than isolated NWs[7] or larger-pitch NWAs,[8, 9] which scatter or diffract light into off-specular directions. Hence, control over light scattering is obtained by patterning in the subwavelength regime, which has not been previously demonstrated for NWA photovoltaics. In addition, most of the incident light is predicted to reflect at wavelengths below 450 nm (not shown), suggesting that an antireflective coating will further increase absorption.

4.3 Absorptance Calculations for Nanohole Arrays

To calculate the absorptance for the nanohole arrays (NHAs), we perform similar RCWA calculations on a two-dimensional periodic model.[10] To reduce the computational load and obtain results within a reasonable time, we simplify the optical model so that only 3 layers are required, and use 49 Fourier modes in the calculation. The top SiO_2 layer has vacuum-filled square nanoholes, sits atop a Si layer with square nanoholes infilled with SiO_2, and that in turn covers an underlying SiO_2 layer with no overetch pits.

Here the holes are 12 nm in size and the pitch is again 32 nm as before, and layer thicknesses are derived from the ellipsometry measurements. This optical model is suggested by the cross-sectional transmission electron microscopy images in the previous chapter, where the oxide sheath around the silicon has almost completely infilled the gaps between the silicon bars. Using this optical model, the calculated absorptance of the square lattice NHAs is shown in figure 4-2 along with that of the film. The NHA absorptance lies above that of the film for much of the wavelength range shown. Here, we observe no polarization dependence, and all the TE and TM curves lie atop each other. This is to be expected from the 4-fold symmetry of the square nanohole lattice, and because all phases in this system are optically isotropic.

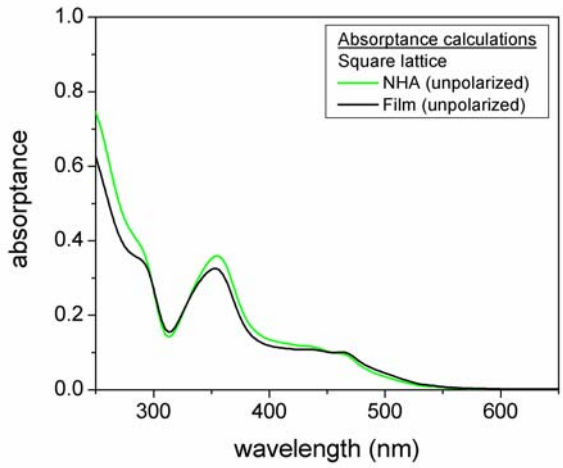

Figure 4-2. Calculated absorptances of square lattice nanohole array and film.

As we have noted previously, the exact choice of the sidewall profile does not impact the calculated results strongly, as long as the period and size of the nanoholes are captured correctly. In our experience, this model adequately captures the essential

characteristics of the material, and minor model modifications do not have a strong effect on the calculated absorptance. In figure 4-3 we show the effect of changing the infill material from SiO_2 to void and that of rounding the SiO_2-filled holes, compared to the original square SiO_2-filled nanohole array. Either modification results in a minor, practically negligible effect on the calculated absorptance. Therefore, we conclude that hole shape and infilling inhomogeneities in the sample have merely a minor impact on the absorptance behavior.

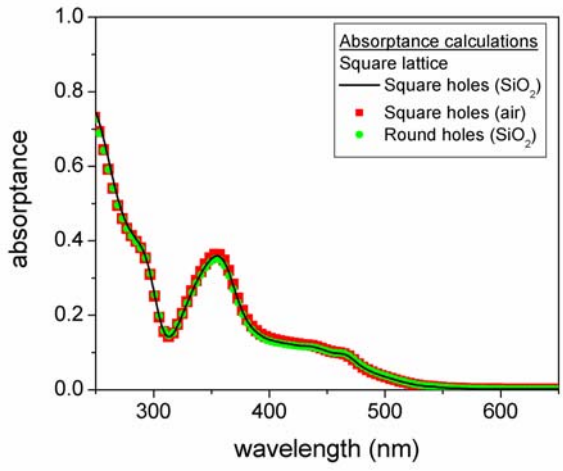

Figure 4-3. Calculated absorptances for square lattice nanohole arrays with small model modifications.

In figure 4-4 we plot the absorptance calculations for SiO_2-filled NHAs with rectangular lattices, which are only 2-fold symmetric. For sufficiently anisotropic lattices, the polarization dependence reappears, and we find that ratio of more than about 4:1 between the *x*- and *y*-periods is required to see strong birefringence. For this example shown, the *x*-period is 4.88 times that of the *y*-period. Here the illumination geometry is such that the plane of incidence is perpendicular to the long period, so that TE- (electric

field parallel to long period) and TM-polarized light (magnetic field parallel to long period) continue to have similar meaning as before. As the ratio of pitches increases, the splitting of the TE and TM curves becomes more evident, indicating that the material becomes more birefringent with an increase in anisotropy. It is clear that clumping of holes or bars can strongly impact the absorptance if the average periodicity of the material changes, even when clumping occurs preferentially in just one direction.

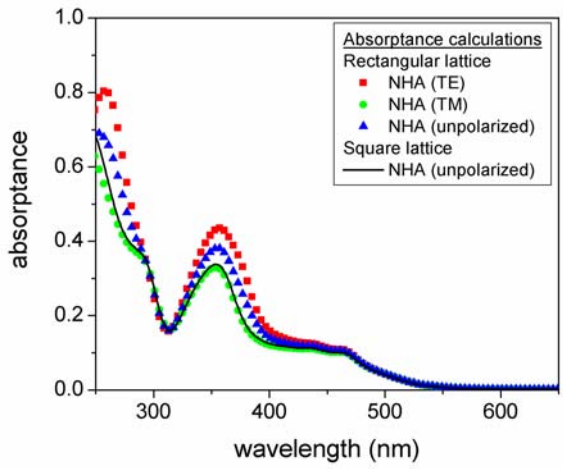

Figure 4-4. Calculated absorptances for a rectangular lattice nanohole array with SiO_2-filled rectangular holes.

4.4 Effective medium approximations

Our nanostructure features are deep in the subwavelength regime, and because the light wavelengths (400 – 700 nm) are much larger than the nanostructure pitch (32 nm), one expects the material to behave like a homogeneous optical material. Hence, the material can be approximated with effective optical constants. Given that we have already performed full RCWA calculations and asserted that these nanostructures behave

as homogeneous optical materials, we now turn to examine the accuracy of the effective medium approximation for our material.

4.4.1 Rytov's Approximation

A number of effective medium approximations (EMAs) such as the Bruggeman or Maxwell-Garnett EMAs are commonly employed for random homogeneous materials, but are not strictly suitable for periodic structures. For structures containing two phases A and B with periodicity in a single dimension, Rytov[11] has produced well-known analytical forms for the effective indices for each polarization: $n_{eff}^{TE} = fn_A + (1-f)n_B$ and $n_{eff}^{TM} = (f/n_A + (1-f)/n_B)^{-1}$, where TE- and TM-polarizations are defined according to the grating physics convention as before. These are suitable when the light wavelength is much larger than the structural pitch. When the light wavelength becomes comparable to the pitch, Rytov's approximations become inaccurate and the wave equation must be solved directly. Here we search for an approximation that approaches the accuracy we obtain from RCWA, yet is computationally inexpensive.

4.4.2 Lifante's Effective Medium for 1-D Gratings

Consider an ideal nanowire array (NWA) consisting of a periodic grating of silicon nanowires with the gaps filled by silicon dioxide. Following Lifante,[12] we can write the electric and magnetic fields of a plane electromagnetic wave propagating along z at normal incidence to the surface as $\mathbf{E}(\mathbf{r},t) = \mathbf{E}(x)\exp(i\omega t - \beta z)$ and $\mathbf{H}(\mathbf{r},t) = \mathbf{H}(x)\exp(i\omega t - \beta z)$. Here $\mathbf{E}$ and $\mathbf{H}$ are the electric and magnetic field vectors, ω

is the angular frequency of the light, and the propagation constant $\beta = k_0 n_{eff} = 2\pi n_{eff} / \lambda$ with wavevector k_0, effective refractive index n_{eff} and the free space light wavelength λ. We wish to solve the wave equation for light $[\nabla^2 - (1/c^2)\partial^2/\partial t^2]\mathbf{E} = 0$ or $[\nabla^2 - (1/c^2)\partial^2/\partial t^2]\mathbf{H} = 0$ so as to obtain the effective refractive index.

There are two independent polarizations that we will consider. The first is the case of transverse electric (TE) polarization when the electric field is polarized perpendicular to the grating vector (and parallel to the nanowires). The wave equation becomes $d^2E_y/dx^2 + [k_0^2 n^2(x) - \beta^2]E_y = 0$ where E_y and dE_y/dx are continuous. The second case of transverse magnetic (TM) polarization, when the electric field is polarized along the grating vector (and perpendicular to the nanowires) yields an analogous equation for the magnetic field $d^2H_y/dx^2 + [k_0^2 n^2(x) - \beta^2]H_y = 0$ with H_y and $(1/n^2)dH_y/dx$ continuous. Both of these differential equations can be solved as boundary value problems by imposing periodic boundary conditions and continuity requirements. We find that even for the shortest wavelengths, the calculated solutions for the field amplitudes remains nearly constant over the entire grating period with variation of <15% over the entire period (not shown). This indicates that the irradiation wavefront remains nearly planar at the surface, as it should for homogeneous materials and suggests that the Rytov approximation should be quite close. Repeating this for a range of wavelengths, we calculate the effective index for our nanowires and compare it to the analytical Rytov estimates in figure 4-5. As can be seen, departures from Rytov's model are relatively modest for TE-polarization but more severe for TM-polarized light especially at shorter wavelengths.

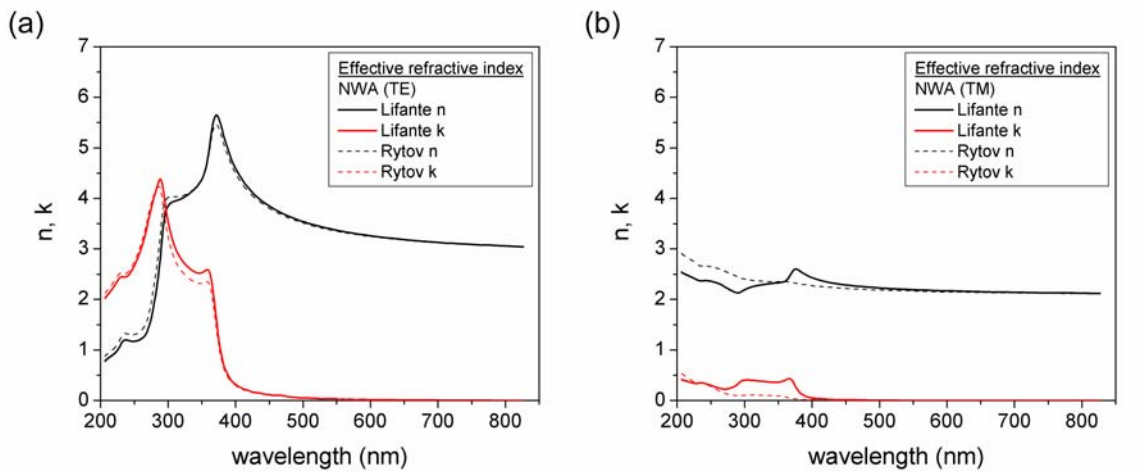

Figure 4-5. Effective refractive indices for SiO_2-filled nanowire array devices under (a) TE- and (b) TM-polarized light.

4.4.3 Lifante's Effective Medium for 2-D Gratings

For biperiodic samples the problem is more involved, since the wave equation is now two-dimensional:

$$d^2E(x,y)/dx^2 + d^2E(x,y)/dy^2 + [k_0^2 n^2(x,y) - \beta^2]E(x,y) = 0\,.$$

Lifante has shown that for long wavelengths compared to the structure periodicity, the biperiodic structure can be considered as a crossed superposition of one-dimensional periodic structures. We follow Lifante's approximate factorization of the wave equation $E(x,y) = \Theta(x,y)\Phi(y)$, and assume that the function $\Theta(x,y)$ has a slow variation in y (so that its derivatives in y vanish). We obtain two decoupled differential equations:

$$d^2\Theta(x,y)/dx^2 + [k_0^2 n^2(x,y) - k_0^2 N^2(y)]\Theta(x,y) = 0\,,$$

$$d^2\Phi(y)/dy^2 + [k_0^2 N^2(y) - \beta^2]\Phi(y) = 0\,,$$

which look like one-dimensional wave equations. The first equation is solved to obtain an effective refractive index $N(y)$, assuming TE polarization and applying the right boundary

conditions and continuity relations. This value is then inserted in the second equation to solve for β, being careful to note that the polarization is now TM and applying the right boundary conditions and continuity relations. In solving these boundary value problems, we take advantage of the speed and simplicity of Rytov's formulas, using them to seed an initial guess for the calculation so as to accelerate convergence to a solution. We find that even for the shortest wavelengths, sequential application of Rytov's approximate formulas (TE-followed by TM-polarization) produces a very good estimate of the effective index as obtained using Lifante's method. The resulting effective indices are plotted in figure 4-6.

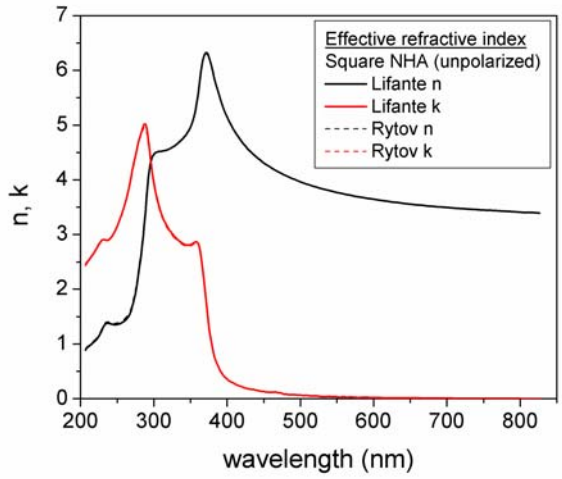

Figure 4-6. Effective refractive index for square-holed, SiO_2-filled, square lattice nanohole array devices under unpolarized light.

4.5 Summary

We apply the rigorous-coupled wave analysis to compute absorptance curves for the nanowire and nanohole array devices, using the structural parameters gleaned from

the characterization studies in chapter 3. These calculations show that the nanowire and nanohole arrays behave like homogeneous materials due to the lack of higher order diffracted intensity in the calculated results. The nanowire arrays are birefringent, while square lattice nanohole arrays are isotropic with no polarization dependence in their absorptance. The absorptances for modified nanohole arrays were also calculated, and changing the nanohole shape or the infill material did not significantly change the absorptance. Hence we conclude that local heterogeneities in the nanohole shape do not affect the absorptance strongly. However, when the periodicity of the nanoholes was changed, the resulting absorptances were affected even when the changes were restricted to a single dimension. Below about period ratios of 2:1 the rectangular nanohole arrays remain close to isotropic, but strongly birefringent behavior appears in rectangular nanohole arrays when the ratio exceeds about 4:1. This indicates that changes in periodicity, such as by clumping of holes or bars, can quickly change the absorptance behavior of nanohole arrays.

The RCWA calculations are computationally intensive, especially for structurally complicated or detailed structures, so we sought to obtain an effective medium description of these nanowire and nanohole arrays. Because these nanostructures are patterned in the deep subwavelength regime, we were able to obtain estimates of the effective refractive indices using Rytov's analytical approximations and compared them to Lifante's approximate solution of the wave equation. Both of these approximations are accurate in the long wavelength limit, but Lifante's formulation enables a good estimate of the effective index at shorter wavelengths where Rytov's approximation is inaccurate.

The results also confirm that the physical picture of these nanostructures as homogeneous optical materials is appropriate.

4.6 References

1. Rathgen, H. MRCWA — Multilayer Rigorous Coupled Wave Analysis Home Page. http://mrcwa.sourceforge.net/ (May 15, 2010).

2. Moharam, M. G.; Pommet, D. A.; Grann, E. B.; Gaylord, T. K., Stable implementation of the rigorous coupled-wave analysis for surface-relief gratings: enhanced transmittance matrix approach. *Journal of the Optical Society of America A* **1995,** 12, 1077.

3. Sun, C.-H.; Min, W.-L.; Linn, N. C.; Jiang, P.; Jiang, B., Templated fabrication of large area subwavelength antireflection gratings on silicon. *Applied Physics Letters* **2007,** 91, 231105.

4. Chen, Y.-B.; Zhang, Z. M.; Timans, P. J., Radiative properties of patterned wafers with nanoscale linewidth. *Journal of Heat Transfer* **2007,** 129, 79-90.

5. Sun, C.-H.; Jiang, P.; Jiang, B., Broadband moth-eye antireflection coatings on silicon. *Applied Physics Letters* **2008,** 92, 061112.

6. Hench, J. J.; Strakoš, Z., The RCWA method — A case study with open questions and perspectives of algebraic computations. *Electronic Transactions on Numerical Analysis* **2008,** 31, 331.

7. Cao, L.; White, J. S.; Park, J.-S.; Schuller, J. A.; Clemens, B. M.; Brongersma, M. L., Engineering light absorption in semiconductor nanowire devices. *Nature Materials* **2009,** 8, 643.

8. Kelzenberg, M. D.; Boettcher, S. W.; Petykiewicz, J. A.; Turner-Evans, D. B.; Putnam, M. C.; Warren, E. L.; Spurgeon, J. M.; Briggs, R. M.; Lewis, N. S.; Atwater, H. A., Enhanced absorption and carrier collection in Si wire arrays for photovoltaic applications. *Nature Materials* **2010,** 9, 239.

9. Cao, L.; Fan, P.; Vasudev, A. P.; White, J. S.; Yu, Z.; Cai, W.; Schuller, J. A.; Fan, S.; Brongersma, M. L., Semiconductor nanowire optical antenna solar absorbers. *Nano Letters* **2010,** 10, 439.

10. Johnson, K. GD-Calc — Grating Diffraction Calculator. http://software.kjinnovation.com/GD-Calc.html (October 18, 2011).

11. Rytov, S. M., Electromagnetic properties of a finely stratified medium. *Soviet Physics JETP* **1956,** 2, 466.

12. Lifante, G., Effective index method for modeling sub-wavelength two-dimensional periodic structures. *Physica Scripta* **2005,** T118, 72.

Chapter 5: Photovoltaic Device Measurements

In this chapter we describe the photovoltaic measurements performed on the nanowire and nanohole array devices. We compare their performance to the control film devices as well as to other devices reported in the literature. Spectral response measurements reveal that these devices can be modeled with bulk optical constants to accurately predict their absorptance. We conclude by estimating the internal quantum yield of the most well-ordered devices.

5.1 Illumination System

Our illumination system consists of an Oriel 150 W Xe arc lamp source coupled at *f*/4 through a home-built cut-on filter changer to an Oriel MS257 monochromator (Newport Corp., Stratford, CT). The divergent output from the monochromator was collimated into a ~1 cm diameter spot at the sample plane using a plano-convex $f = 75$ mm lens (Thorlabs, Newton, NJ). We selected "UV-grade" fused silica for all optical elements to maximize transmission of the ultraviolet wavelengths.

5.1.1 Irradiance Calibrations

The irradiance calibration reference is a Hamamatsu S1337-1010BQ silicon photodiode (Hamamatsu, Bridgewater, NJ), calibrated between 250 and 1100 nm to

NIST-traceable standards (Opto-Cal, Lakeside, CA) and mounted behind a 500 μm diameter precision pinhole (Edmund Optics, Barrington, NJ). The wavelength-dependent irradiance was measured in the center of the collimated beam at the sample plane using a 10 nm bandpass in steps of 1 nm. We have also measured the irradiance spectrum with an uncoated Glan-Thompson linear polarizer (Thorlabs, Newton, NJ) mounted just before the detector and find that there is only a slight polarization introduced by the illumination system, which we shall ignore in the following analysis.

5.1.2 Wavelength Calibrations

Wavelength calibrations were regularly performed, often before each set of measurements, using the sharp emission lines from a Hg(Ar) pen-style lamp (Newport, Stratford, CT) at the input of the monochromator and the reference photodiode at the sample plane. For each of the gratings used, the monochromator was scanned in 0.1 nm steps in the vicinity of a strong emission line. The position of the peak was used to calibrate the monochromator wavelength readout, and was typically reproducible to ~0.1 nm. At the end of each wavelength calibration, monochromator slit functions were also measured at 10 nm bandpass in steps of 0.1 nm to characterize the instrumental broadening of the illumination system. The slit functions were nearly perfectly triangular and identically wide for all gratings used, indicative of a well-aligned optical system.

5.2 Photovoltaic Measurements

For optical characterization, the principal device was mounted on and wire-bonded to a chip carrier before loading into the cold finger of an optical cryostat

equipped with 1” diameter windows for sample illumination. After wavelength and irradiance calibrations, spectral response measurements were performed at 300 K under vacuum (~10^{-5} torr), using the collimated output from a monochromated Xe arc lamp. A monochromator bandpass of 10 nm was used and the illumination wavelength was scanned between 250 and 800 nm in 1 nm steps while the spectral response data were collected. Polarization-resolved spectral response measurements were also performed by illuminating the devices through an uncoated Glan-Thompson linear polarizer and measuring the photocurrent at several polarizer settings. The data consist of photocurrent I measurements made with a Model 6430 sourcemeter at zero applied bias (Keithley Instruments, Cleveland, OH), which yield the spectral responsivity R via the relation $R(\lambda) = I(\lambda) / [Y \times E(\lambda)]$, where E is the calibrated irradiance of the incident illumination. The active light-collecting area is $Y = L \times W$, determined by the physical width of the device W and the minority carrier diffusion length L. The spectral responsivity is transformed into the external quantum efficiency (EQE) using the equation $EQE(\lambda) = (1240 \text{ W nm A}^{-1}) \times R(\lambda) / \lambda$. Additionally, current-voltage scans were performed in the dark and under standard AM1.5G illumination to characterize the photovoltaic properties of the NWA or NHA and film diodes. Complete photovoltaic characterization of selected devices were performed to extract short-circuit currents, open-circuit voltages, and fill factors, while an abbreviated measurement protocol was followed for other devices (no fill factor).

5.3 Nanowire Array Devices

A few sets of thin film and NWA devices were fabricated. The devices described below were chosen for optical characterization because they appeared, by light microscopy inspection, to be the most homogeneous. The devices chosen were selected for the absence of irregularities due to fabrication variability, so as to avoid artifacts in the measured optical data.

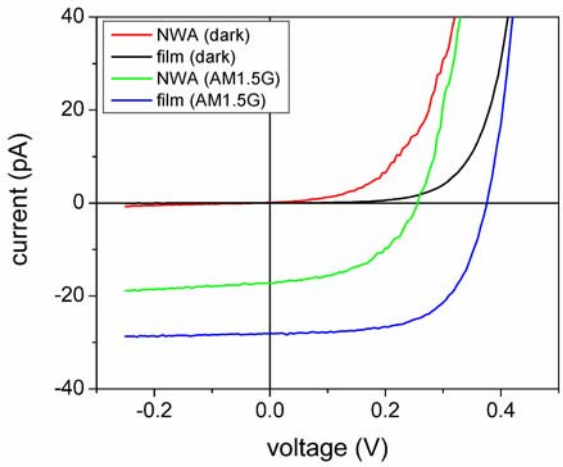

Figure 5-1. Dark and lit I-V curves for a representative pair of NWA devices.

5.3.1 Broadband Photovoltaic Measurements

Figure 5-1 shows clear diode responses from a set of devices with high-dose doping (3.8×10^{13} cm^{-2} B^{+}) in the device regions. These higher-doped nanowire array devices generate I_{sc} = 17 pA and V_{oc} = 0.26 V with FF = 0.50, while the higher-doped film devices develop I_{sc} = 28 pA and V_{oc} = 0.37 V with FF = 0.62. However, the higher-doped nanowire arrays were of poorer structural quality and were less amenable to optical modeling. In the following discussion we focus on the lower-doped (3.8×10^{10} cm^{-2} B^{+}) principal device.

Table 5-1. Measured photovoltaic parameters of nanowire array devices, compared to reported values for similar devices.

Sample	I_{sc} (pA)	J_{sc} (mA cm^{-2})	V_{oc} (V)	*FF*	n_{lit}	n_{dark}	Description
3.8×10^{13} cm^{-2} B^{+} dose							
NWA	17	-	0.26	0.50	2.2	2.7	10 μm long
NWA	17	-	0.34	0.60	1.8	1.8	10 μm long
NWA	17	-	0.34	0.55	2.2	1.9	25 μm long
Thin Film	28	-	0.37	0.62	1.5	1.9	10 μm long
Thin Film	27	-	0.36	0.60	1.6	1.8	10 μm long
Thin Film	27	-	0.37	0.62	1.8	1.7	25 μm long
NWA	18	-	0.26	-	-	-	25 μm long
NWA	19	-	0.38	-	-	-	50 μm long
NWA	19	-	0.35	-	-	-	100 μm long
Thin Film	29	-	0.40	-	-	-	25 μm long
Thin Film	30	-	0.40	-	-	-	25 μm long
Thin Film	29	-	0.39	-	-	-	100 μm long
3.8×10^{10} cm^{-2} B^{+} dose							
NWA[a]	26	2.6	0.37	-	-	-	10 μm long
Film[a]	60	3.0	0.46	-	-	-	10 μm long
Literature values							
Kelzenberg[1]	-	5.0	0.19	0.40	-	3.6	Axial Schottky
Kempa[2]	3.5	-	0.12	-	1.78	-	Axial p-n
Kempa[2]	14.0	-	0.24	-	-	-	Axial p-i-n, i=2 μm
Kempa[2]	31.1	3.5	0.29	0.51	1.28	-	Axial p-i-n, i=4 μm
Garnett[3]	-	4.28	0.29	0.33	-	2.1	Radial p-n
Tian[4]	503	23.9	0.26	0.55	1.86	1.96	Radial p-i-n

a) NWA and film devices in Figure 5-2.

For a device that appeared the most perfect under optical and SEM imaging, full optical characterization, as well as cross-sectioning and TEM imaging to establish the structural details of the device for the optical model, were carried out. These results were discussed in Chapter 3 and were the basis for the optical models developed in chapter 4. This was the principal device studied here (NWA: J_{sc} = 2.6 mA cm^{-2}, V_{oc} = 0.37 V; film: J_{sc} = 3.0 mA cm^{-2}, V_{oc} = 0.46 V). For other devices, the photovoltaic device characteristics (with and without illumination) were fully or partially measured. Table 5-1 is a summary of our nanowire array and film devices, compared to similar devices in the literature.

Both NWA and film devices perform as good rectifying diodes in the dark and exhibit clear photovoltaic response under 1 Sun AM1.5G irradiation (see figure 5-1). The NWA devices show more variability in their properties, while the film devices are practically identical to each other. Our devices are comparable in performance to other examples[2-5] of silicon nanowire photovoltaic devices reported in the literature (table 5-1). Where possible, we have calculated the short-circuit current density J_{sc} using the projected active area $Y = L \times W$ of the device. Ideality factors n_{lit} and n_{dark} were obtained by fitting lit and dark I-V measurements to the diode equation $I = I_0 [\exp(qV/nk_BT) - 1]$ in the low forward bias region (up to ~0.4 V). Additionally, measured photovoltaic characteristics do not vary with device length as the measured minority carrier diffusion lengths (discussed below) are shorter than the geometrical lengths of the devices.

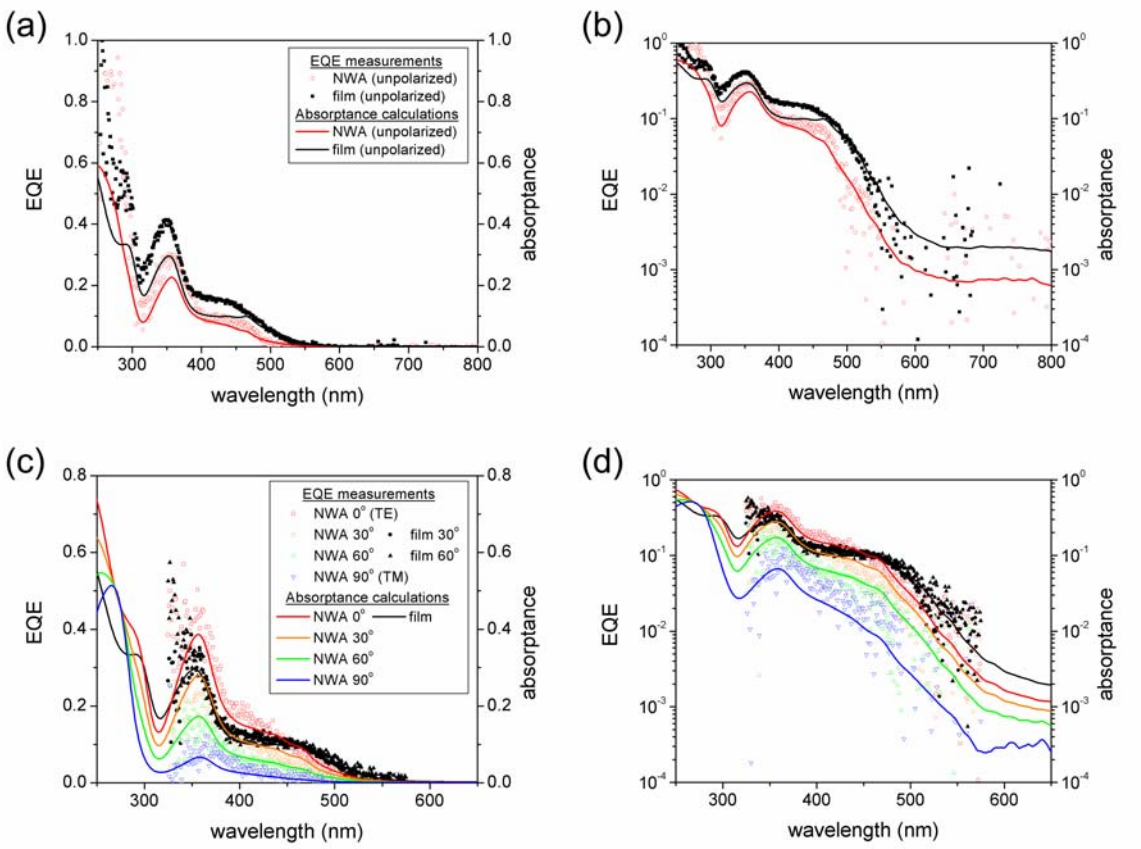

Figure 5-2. (a, b) External quantum efficiencies and (c, d) Polarization-resolved external quantum efficiencies of nanowire array and film devices on linear and semilogarithmic plots.

5.3.2 Spectral Response Measurements

The external quantum efficiencies of film and NWA devices for unpolarized illumination (symbols) are plotted in figure 5-2a, and are strikingly similar to the calculated absorptances (lines) from rigorous coupled-wave analysis (RCWA). The agreement is even more impressive when plotted logarithmically (figure 5-2b), given the simplicity of the optical models. Polarization-resolved external quantum efficiencies (see figure 5-2c,d) further support our interpretation of the NWA devices as uniaxial birefringent materials. The external quantum efficiency of the NWA devices changes by an order of magnitude between the TE- and TM-polarizations around 360 nm (colored

hollow symbols), as predicted by RCWA calculations (colored lines). On the other hand, the film devices do not exhibit large variations in their spectral response as the polarization is changed (black solid symbols), as predicted for an isotropic medium (black line). Scanning photocurrent measurements with a scanning near-field optical microscope (see chapter 3) give lower estimates for the minority carrier diffusion length L. For the bulk film devices, $L_{film} \geq 200$ nm, while for the NWA devices, $L_{NWA} \geq 100$ nm. As a check, we note that energy conservation also imposes a lower limit on L, since the internal quantum efficiency $IQE = EQE \div A$ cannot exceed unity at $h\upsilon < 2E_g$. These lower limits correspond exactly to the estimates obtained from the scanning photocurrent measurements. To produce figure 5-2, we have applied the lower limiting values for L_{film} = 200 nm and L_{NWA} = 100 nm; the reader should divide the EQE values by 2 (bulk film) or 3 (NWA) to apply the upper limits on L.

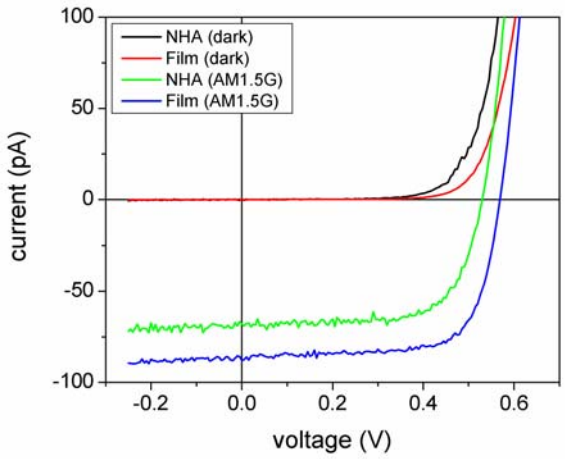

Figure 5-3. Dark and lit I-V curves for a representative pair of NHA devices.

5.4 Nanohole Array Devices

5.4.1 Broadband Measurements

Similar measurements were performed for the NHA devices. In early devices using the same passivation protocol as the nanowires, we observed similar performance for the dark and lit I-V characteristics. In later devices using our best passivation protocol (see chapter 2), we were able to drastically improve the photovoltaic performance of both the NHA and film diodes.

Table 5-2. Measured photovoltaic parameters of nanohole array devices.

Sample	I_{sc} (pA)	J_{sc} (mA cm^{-2})	V_{oc} (V)	FF	n_{lit}	n_{dark}	Description
3.8×10^{10} cm^{-2} B^+ dose, RCA+RTO+FGA passivation							
NHA1	37	-	0.29	0.42	-	-	10 μm long
NHA2	45	-	0.30	0.43	-	-	10 μm long
Film1	66	2.6	0.49	0.54	-	-	10 μm long
Film2	70	2.5	0.49	0.53	-	-	10 μm long
3.8×10^{10} cm^{-2} B^+ dose, HF-last RCA+RTO+POA+FGA passivation							
NHA3[b]	68	2.3	0.53	0.70	1.8	1.7	10 μm long
Film3[b]	88	2.3	0.57	0.71	1.6	1.5	10 μm long
Literature values							
Peng[5]	-	32.2	0.5666	0.522	-	-	Bulk device

b) NHA and film devices in Figure 5-3.

In figure 5-3 we show one such set of improved devices measured in the dark and under standard 1 Sun AM1.5G illumination (NHA: J_{sc} = 2.3 mA cm^{-2}, V_{oc} = 0.53 V, FF = 0.70; film: J_{sc} = 2.3 mA cm^{-2}, V_{oc} = 0.57 V, FF = 0.71). The NHA performance is almost on par with the film device, both having comparable short-circuit current densities, open-circuit voltages and fill factors. These devices are less than 10 nm thick, and hence have low current densities due to the low spectrum-integrated absorptance, yet the high fill factors and open-circuit voltages resulting from the improved passivation are comparable to or exceed those from a comparable bulk device. In table 5-2 we summarize the results from these devices.

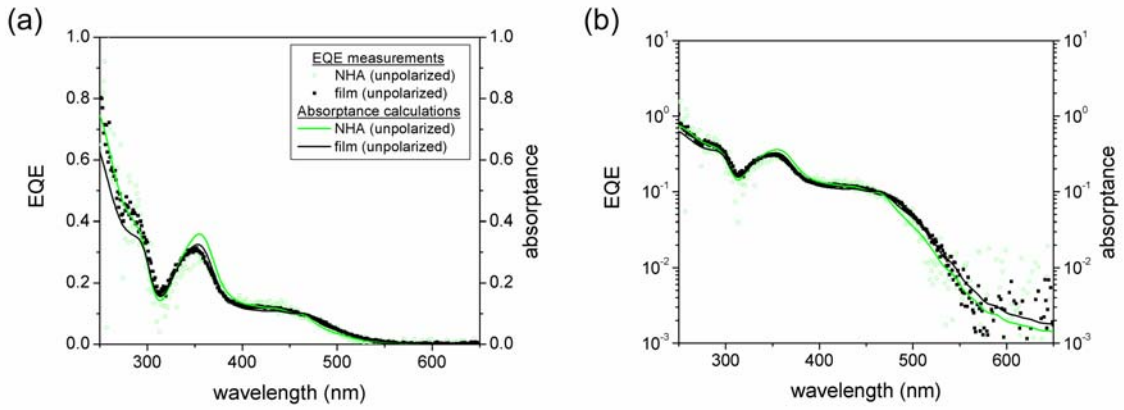

Figure 5-4. (a, b) External quantum efficiencies and absorptances of well-ordered nanohole array (NHA3) and film (Film3) devices for unpolarized collimated illumination plotted on linear and semilogarithmic scales, showing a good fit spanning several orders of magnitude.

5.4.2 Spectral Response Measurements

Spectral response measurements were also performed for these NHA devices and those from a highly homogeneous sample (NHA3) are shown in figure 5-4a,b. Here the agreement between the external quantum efficiencies and the calculated absorptances are

excellent. On the other hand, similar plots for the other two samples (NHA1 and NHA2) did not produce good matches. In chapter 4, we noted that perturbations in the hole periodicity due to clumping changed the computed nanohole array absorptance. The nanohole arrays are particularly sensitive to this type of defect, and we show below that these defects can account for the discrepancies observed with the disordered samples.

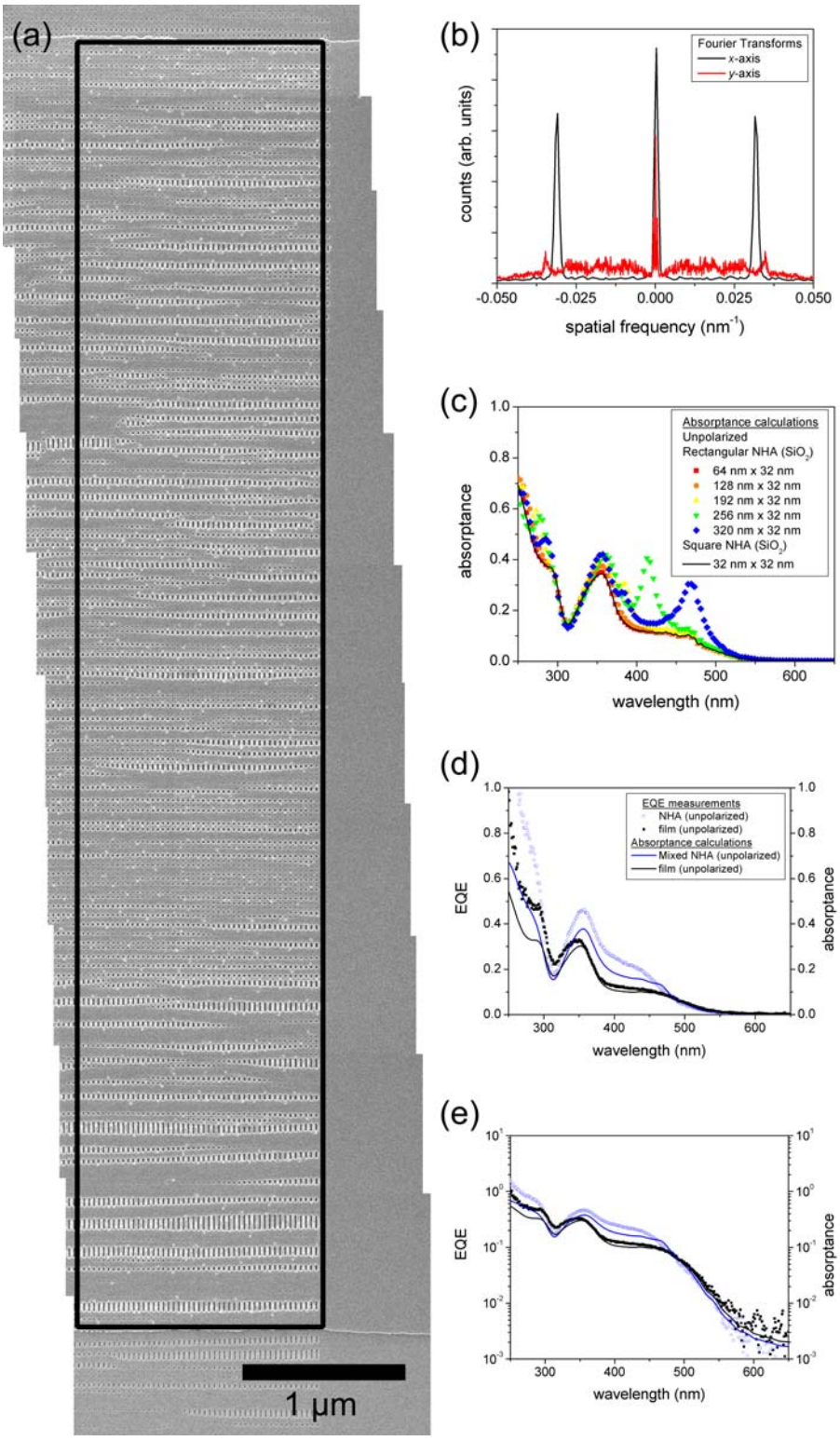

Figure 5-5. (a) Scanning electron micrograph of disordered nanohole array (NHA2). (b) Fourier transforms of boxed region in the horizontal and vertical directions. (c) Calculated absorptances for component nanohole lattices. (d, e) Weighted sum of component absorptances plotted on linear and semilogarithmic scales.

During scanning electron microscopy experiments on these disordered samples we observed significant clumping of the bars and holes (Figure 5-5a). Taking the two-dimensional Fourier transform of the boxed region, sharp peaks were isolated in the horizontal direction corresponding exactly to the design period of 32 nm (black line in figure 5-5b). On the other hand, a diffuse spectrum was obtained for the vertical direction, indicating disorder in the nanohole array along this axis (red line in figure 5-5b). Using RCWA (chapter 4), we calculated the unpolarized absorptances for component rectangular nanohole lattices with vertical-to-horizontal period ratios ranging between 0.7 to 10. The absorptances of selected rectangular NHAs (colored points) are plotted in figure 5-5c along with that predicted for the square NHA (black line). The rectangular NHAs have strong absorptance peaks between 350 to 500 nm that are absent in the square NHA, suggesting that the enhanced EQE at these wavelengths arises from increased absorptance in rectangular NHA domains created by nanohole lattice disorder.

One can imagine that given a mix of nanohole regions with varying periodicities, the overall absorptance is an average of the constituent domains, as long as the domains are well mixed on the wavelength scale of the incident light. Indeed, when all of the component absorptances are summed according to their relative weights in the vertical Fourier transform, the resulting calculated absorptance approaches the measured experimental EQE (Figure 5-5d,e). To obtain these weights, we first calculate the spatial frequency (in nm^{-1}) corresponding to each period ratio. We then split the Fourier spectrum into bins, with bin edges defined at the midpoints between each component spatial frequency, and calculated the average spectrum value in each bin. Since each unit

of spatial frequency corresponds to a wider swath of real space at lower frequencies, we correct for this disproportionate weighting factor by dividing the average spectrum value in each bin by the spatial frequency at the center of the bin.

5.5 Design Rules for Enhanced Absorption

We have shown earlier that spatial disorder in NHA1 and NHA2 is responsible for the enhanced absorptance and external quantum efficiency in these samples. This result suggests several approaches for absorptance engineering in NHAs. For example, if an increase in broadband absorptance is desired for increased photovoltaic performance, one could introduce disorder into square NHAs along a single axis, just as we have done here, so that the component rectangular NHAs created by disorder increase absorptance in the wavelength range of interest. Alternatively, the NHA could incorporate discrete domains of rectangular NHAs, each of which are designed for a specific absorptance profile, and which are well mixed on the wavelength scale of interest. On the other hand, if tunable birefringence and absorptance are desired for detector applications, a specific rectangular NHA could be patterned to enhance response over that of the square NHA. For example, multicolor polarization-sensitive detectors could be patterned on a single substrate by simple manipulation of the rectangular NHA periods and axes.

5.6 Estimates of Internal Quantum Efficiency

We can estimate the internal quantum efficiencies $IQE = EQE \div A$ by dividing the measured external quantum efficiency EQE by the calculated absorptance A. This calculation is particularly problematic for disordered devices as RCWA cannot properly

account for spatial disorder. Therefore, we restrict the following discussion to the best and most well-ordered samples. In figure 5-6a and figure 5-6b we plot these IQE estimates for a nanowire and a nanohole array device. There are unexpected sharp kinks and shoulders in the curves that occur most often near turning points in the absorptance spectra, and that suggest that the optical models are not completely accurate. Nonetheless, the data for the film devices follow the general trend reported for silicon, rising somewhat at wavelengths of <400 nm to reach about 1.5 at 250 nm.[6] The nanowire and nanohole arrays appear to follow this general trend as well. Given the large amount of noise in these data, we cannot conclude if nanostructuring photovoltaics affects the quantum yield in a significant way. If there is any effect, it must be rather minor.

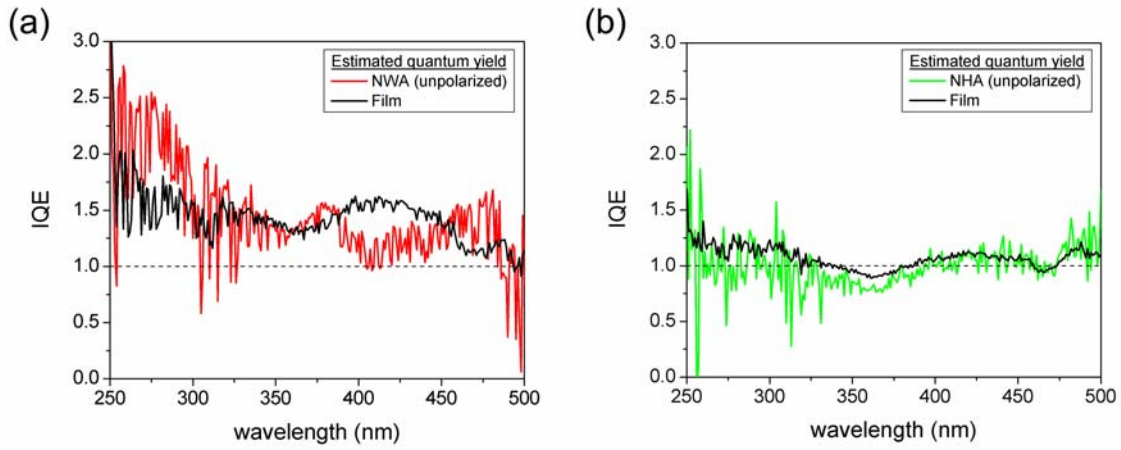

Figure 5-6. Internal quantum efficiency estimates obtained by dividing the measured external quantum efficiency by the calculated absorptance for (a) nanowire and (b) nanohole array device.

5.7 Summary

We have described measurements on nanowire and nanohole array photovoltaic devices. The nanowire array devices show strong birefringence in their absorptance, as predicted from RCWA calculations and confirmed experimentally with polarization-

resolved spectral response measurements. On the other hand, the nanohole array devices have an isotropic optical response except when their periodicities are changed along one dimension preferentially, as can happen in disordered samples. In our best devices, photovoltaic performance rivals or exceeds values reported in the literature for comparable samples.

The excellent match between the measured EQE and the absorptance for the nanowire and nanohole arrays implies that we can accurately predict the optical characteristics of such materials from bulk optical constants, at least down to the nanostructure dimensions investigated here. In addition, because the array features are so small compared to visible light, we can treat the array as a homogeneous thin film with effective refractive indices for each polarization (see chapter 4). The advantage of such an approach is that optical stacks containing these nanostructured films can be accurately modeled using standard thin film optics. Nanostructuring at extreme length scales thus paves the way toward completely tunable optical properties, down to the ultraviolet. For example, tunable birefringence as demonstrated in this work, can find applications as polarization-sensitive detectors or emitters, waveplates, and in power-generating ultrathin semitransparent films on windows.

On the other hand, within the limits of our analysis, we cannot determine if these nanostructure array photovoltaics outperform bulk silicon in terms of quantum yield. We conclude that if such an effect exists, it must be rather small, at least for the conditions investigated here. These nanostructures behave similarly to the “bulk” film material in terms of quantum yield.

5.8 References

1. Kelzenberg, M. D.; Turner-Evans, D. B.; Kayes, B. M.; Filler, M. A.; Putnam, M. C.; Lewis, N. S.; Atwater, H. A., Photovoltaic measurements in single-nanowire silicon solar cells. *Nano Letters* **2008,** 8, 710.

2. Kempa, T. J.; Tian, B.; Kim, D. R.; Hu, J.; Zheng, X.; Lieber, C. M., Single and tandem axial p-i-n nanowire photovoltaic devices. *Nano Letters* **2008,** 8, 3456.

3. Garnett, E. C.; Yang, P., Silicon nanowire radial p-n junction solar cells. *Journal of the American Chemical Society* **2008,** 130, 9224.

4. Tian, B.; Zheng, X.; Kempa, T. J.; Fang, Y.; Yu, N.; Yu, G.; Huang, J.; Lieber, C. M., Coaxial silicon nanowires as solar cells and nanoelectronic power sources. *Nature* **2007,** 449, 885.

5. Peng, K.-Q.; Wang, X.; Li, L.; Wu, X.-L.; Lee, S.-T., High-performance silicon nanohole solar cells. *Journal of the American Chemical Society* **2010,** 132, 6872.

6. Kolodinski, S.; Werner, J. H.; Wittchen, T.; Queisser, H. J., Quantum efficiencies exceeding unity due to impact ionization in solar cells. *Applied Physics Letters* **1993,** 63, 2405.